DETERMINATION OF THE CONTROLS ON PERMEABILITY AND TRANSPORT IN SHALE BY USE OF PERCOLATION MODELS

A Thesis

by

IAN BERNARD CHAPMAN

Submitted to the Office of Graduate Studies of
Texas A&M University
in partial fulfillment of the requirements for the degree of

MASTER OF SCIENCE

August 2012

Major Subject: Petroleum Engineering

Determination of the Controls on Permeability and Transport in Shale

by Use of Percolation Models

DETERMINATION OF THE CONTROLS ON PERMEABILITY AND TRANSPORT IN SHALE BY USE OF PERCOLATION MODELS

A Thesis

by

IAN BERNARD CHAPMAN

Submitted to the Office of Graduate Studies of
Texas A&M University
in partial fulfillment of the requirements for the degree of

MASTER OF SCIENCE

Approved by:

Chair of Committee,	Michael King
Committee Members,	Peter Valko
	Yuefeng Sun
Head of Department	A. Daniel Hill

August 2012

Major Subject: Petroleum Engineering

ABSTRACT

Determination of the Controls on Permeability and Transport in Shale
by Use of Percolation Models. (August 2012)
Ian Bernard Chapman, B.S., University of Virginia
Chair of Advisory Committee: Dr. Michael King

A proper understanding of reservoir connectivity is essential to understanding the relationship between the porosity and the permeability within it. Additionally, the construction of an accurate reservoir model cannot be accomplished without this information. While a great deal is known about the connectivity in conventional sandstone systems, little is understood about the connectivity and its resultant properties within shale systems. Percolation theory is a method to describe the global properties of the shale system by understanding the nanometer scale interaction of pore space.

In this study we use both analytical and empirical techniques to further understand shale pore scale interactions as well as global phenomena of the shale system. Construction of pore scale connectivity simulations on lattice and in the continuum allow for understanding relationships between pore topology, system porosity and system permeability. Additionally, questions regarding the role of Total Organic Carbon as well as natural fractures in contributing to shale permeability will be discussed. Analytical techniques are used to validate simulation results regarding the onset of percolation and related pore topology. Finally, time of flight simulation is used to further understand pressure transient behavior in the resulting topological models.

High aspect ratio pores are shown to be the driver of shale permeability as opposed to the low aspect ratio pore space associated with organic matrix. Additionally, systems below the percolation threshold are likely able to produce because the wellbore will often encounter near infinite clusters. Finally, a characteristic volume growth profile is shown for a multi-porosity system whereby each level of porosity displays a corresponding stair step of volume growth in time.

DEDICATION

To my parents, for their support and encouragement

ACKNOWLEDGEMENTS

I would like to thank Dr. Michael King and Dr. Peter Valko for enduring my interminable questions.

NOMENCLATURE

SEM	Scanning Electron Microscopy
TEM	Transmission Electron Microscopy
MICP	Mercury Injection Capillary Pressure
NMR	Nuclear Magnetic Resonance
TOF	Time of Flight

TABLE OF CONTENTS

LIST OF FIGURES

FIGURE Page

CHAPTER I

INTRODUCTION

The factors controlling permeability in shale gas formations are not currently well understood. While in general a porosity-permeability predictor can be built for most lithologies, shale systems present novel problems concerning local connectivity that in turn affect large scale permeability. The industry currently does not have a firm understanding of how well a shale system's pore space is interconnected nor does it have an understanding of which geologic factors and to what extent these factors affect that connectivity. A better understanding of pore scale connectivity can assist in solving problems ranging from estimated ultimate recoverable hydrocarbons to stimulated reservoir volume.

Several tools are used to determine global properties of the shale system. Excluded volume is the first and is related directly to the topology of individual pore space (Balberg et al. 1984). The idea of excluded volume allows us to determine pore shape based solely on large scale permeability. The converse is also true whereby a determination of permeability can be made based solely on the knowledge of individual pore shapes.

In addition to analytical methods, we employ percolation theory coupled with steady state pressure solving techniques to determine system permeability and its relation to pore geometry. By merging knowledge of inorganic matrix pore topology as well as organic matrix topology we are able to construct a method of permeability estimation as a function of pore shape, total system porosity and total organic carbon.

This thesis follows the style of the *SPE Reservoir Evaluation and Engineering*.

CHAPTER II

THEORY

GEOLOGIC FACTORS

In the last several years a great number of attempts have been made to properly characterize both the pore network connectivity and fluid flow characteristics of shale systems (Passey et al. 2010). One of the earliest and most common techniques was to look at optical images of shale thin sections. Quickly it was discovered that this method did not provide the proper resolution to understand the internal structure of a shale system because the optical wavelength was often greater than the pore sizes of the systems under examination. As a result, researchers moved to higher resolution procedures including the use of Scanning Electron Microscopy (SEM) as shown in Figure 2.1 and Transmission Electron Microscopy (TEM) as shown in Figure 2.2. With resolutions on the order of 1 nm, these techniques were able to determine internal shale structures not previously visible. As a result of this process several revelations on the pore structure and connectivity of shale systems were indicated. For instance, isolated pore space visible through SEM appeared to show some connectivity when viewed using TEM (Curtis et al. 2012).

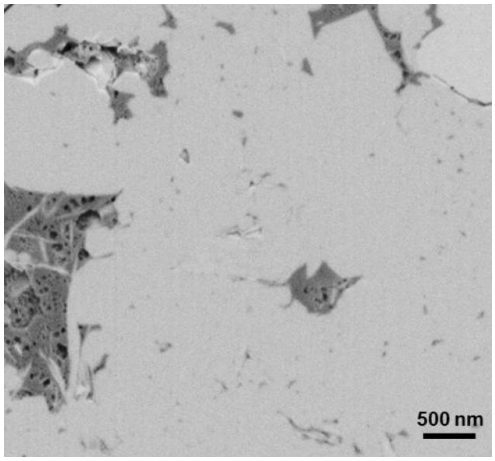

Fig. 2.1 – SEM Image of Kerogen Pores from a Barnett Shale Sample, (Curtis et al. 2012)

However, with only qualitative studies being conducted, they could not say definitively whether their sample exhibited large scale connectivity. Additionally, petrophysical techniques were explored to characterize shale pore size distributions (Curtis et al. 2011). Both Mercury Injection Capillary Pressure (MICP) and Nuclear Magnetic Resonance (NMR) imaging were used; the former to explore pore throat size and the latter pore body radius. Once again, while the techniques accurately characterized pore throats and volumes, no mention is made of large scale connectivity. In other words, these techniques do not allow for the quantification of stranded pore volumes.

Additionally, Curtis et al. mentions the prevalence of kerogen throughout the samples. Once again, while a quantitative description of kerogen pore size and overall porosity are given, no attempt is made to relate TOC to kerogen density in the system or to understand how the kerogen pore space is connected to the larger shale porosity

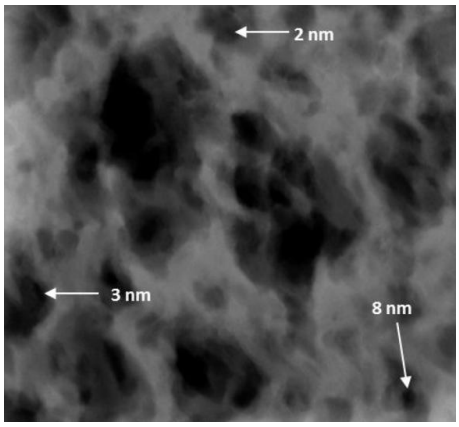

Fig. 2.2 – TEM Image of Barnett Shale Kerogen (Curtis and Ambrose, 2011)

Tests were performed to more accurately describe the shale system using high pressure mercury porosimetry analysis as well as SEM and X-Ray Diffraction. Using MICP indicates a median pore throat diameter of 30 nm with the majority of throats falling in the range of 10-60 nm for a Utica Shale sample (Elgmati et al. 2011). This can be contrasted to a later Haynesville sample showing pore throat diameters of approximately 4-20 nm. Previous studies have shown that MICP slightly underestimates throat sizes and comparison to SEM data is suggested to validate results (Elgmati et al. 2011).

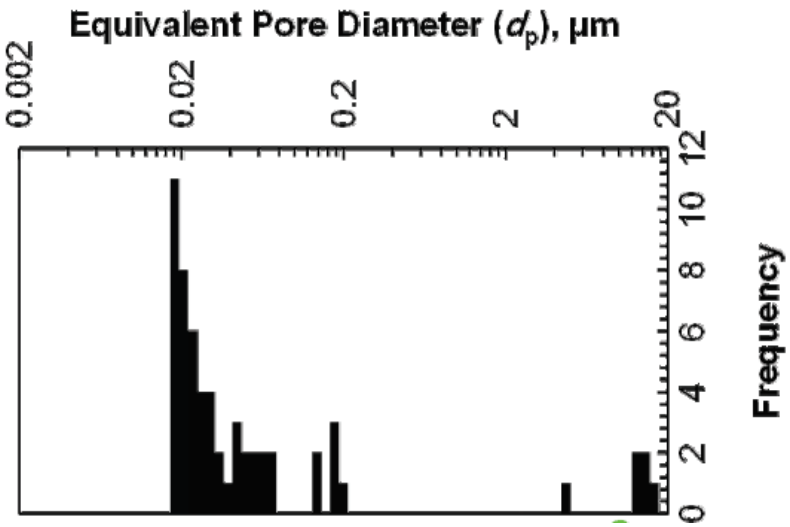

Fig. 2.3- Equivalent Pore Diameter Histogram for Utica Shale Sample, (Elgmati et al. 2011)

We can see in Figure 2.3 above a histogram showing that the largest component of pore diameters occurs slightly below the 0.02 micrometers. Additionally, there appears to be some mesoscopic pore space in the 15-20 micrometer range which may represent natural fracturing or vuggy porosity.

From the pore size distribution, the authors attempt to construct a permeability profile from porosity and pore diameter data using Kozeny's model of fluid flow through cylindrical channels by combining Darcy's law and Poisueille flow where;

$$k = \frac{\varphi * dp^2}{32 * t}$$

The equation above relates k, the permeability of the system to φ, the porosity to dp, the average pore diameter and τ, the tortuosity coefficient. Using this formula the previously described Utica shale sample has a permeability of roughly $4.15 * 10^{-3}$ md or 4.15 µd.

A similar Utica shale sample was also tested using SEM. “Intergranular pore sizes [of the Utica Shale sample] ranged from 15 to 50 nm” (Elgmati et al. 2011). Additionally, some intragranular pore space was recognized with pore throats diameters in the range of 5 nm. Combination of SEM and Energy Dispersive Spectroscopy (EDS) element mapping shows several vuggy pores 2-8 micrometers in diameter with the potential ability to store free gas. Additionally, kerogen is shown to have pore diameters of 5-100 nm and conductive natural fractures with throat openings of 25-50 nm.

Serial sectioning of the Utica Shale sample was used to build a 3D model. As can be seen in Figure 2.4 below, the most common pore size diameter occurred in the 0.03 micrometer size range with equivalent kerogen, permeability, and porosity calculations as shown below.

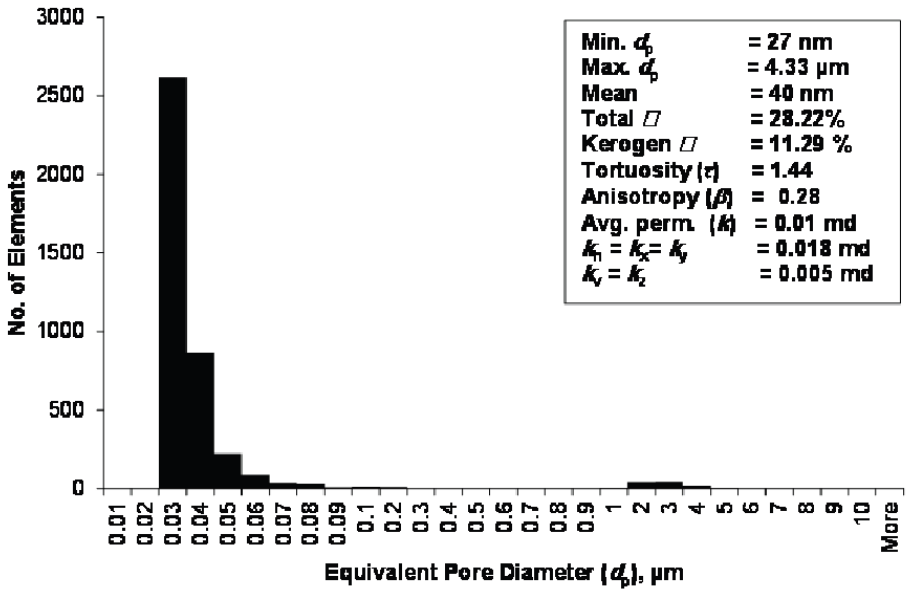

Fig. 2.4- Equivalent Pore Diameter for Fayetteville Shale Sample, (Elgmati et al. 2011)

The internal structure of the shale system contains four types of productive porous media in the gas-shale system: inorganic matrix, organic matrix, natural fractures, and hydraulic fractures (Wang and Reed 2009). Organic matrix in the system is the dominant factor in the storage of both free and adsorbed gas as well as the main transport mechanism for gas in the shale system. Because the organic matrix tends to be oil wet, it allows for single phase fluid flow and low

permeability to water. Despite the relatively small size of organic pores in shale (often as low as 5 nm in diameter), the organic matrix may have porosities as high as 25% which could allow for large scale hydrocarbon transport for a given shale system.

Figure 2.5 below demonstrates that a linear relationship can be derived between TOC and gas content of the shale. This is further broken down into percentages of gas stored as free gas in the inorganic matrix, free gas in the organic matrix and adsorbed gas in the organic matrix.

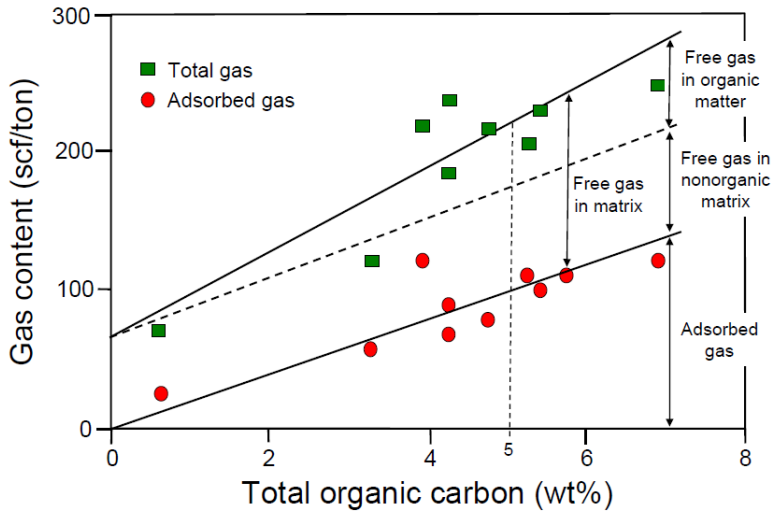

Fig. 2.5 – Adsorbed and Total Gas Content with Respect to TOC in Barnett Shale, (Wang and Reed 2009)

While free gas in the inorganic matrix remains relatively stable despite TOC weight percentages in the shale system, the amount of gas stored in the organic matrix increases dramatically with increases in TOC weight percentages. Despite understanding this relationship, organic matrix connectivity within the larger shale system is still poorly characterized. As a result, even though weight percentages of organic matrix within a system are well known, how well it is dispersed through the system is not. This makes large scale permeability difficult to determine.

In the assessment of several shale samples, it is noted that many factors affect permeability including shale type, porosity, confining pressure and pore pressure (Wang and Reed 2009). While these factors appear to play a dominant role when systematically testing core sample

permeability, it is unclear by how much each factor is affecting the system. Two important notes come from this permeability study. The first is mention that the carbon rich shale systems may have in-situ permeability orders of magnitude greater than their organic lean counterparts. Additionally, the fact that pore networks in organic matter are most likely connected through micro-fractures is first noted (Wang and Reed 2009). Unfortunately, very little evidence is given to support this hypothesis. The authors believe that a bulk permeability including the effects of both micro-fractures and organic matrix is sufficient in the simulation of shale systems. It is our intent to expand on this to accurately describe the geology of the shale system.

Perhaps the most important conclusion comes from the shale reservoir description. The authors describe a hierarchy of system porosity which in turn, leads to a hierarchy of permeability. High permeability in gas shale can most likely form when nano-pores in the organic matter connected by natural micro- and macro-fractures are accessed by hydraulic fractures (Wang and Reed 2009). Additionally, the poorly connected organic matter and diffusion of free gas from inorganic matrix allow for long lasting, relatively low production rates.

As discussed previously, there are several different types of pore structures within a shale system. In general these structures can be divided into inorganic matrix, organic matrix and natural micro fractures. Inorganic matrix makes up the bulk of rock volume but most likely plays the least important role in shale system connectivity. Because shale grain sizes are generally less than 1/256 mm, inorganic matrix pore space is extremely limited. As a result it appears to be too compact for any large scale connectivity of inorganic pore space (Loucks et al. 2009).

The second and perhaps most interesting pore structure to the shale system is the organic matrix. The organic matrix has been given a great deal of scrutiny as of late because of its large volumetric portion in shale samples (Passey et al. 2010). When shale first forms a certain amount of organic matter is deposited along with the inorganic particulate, during diagenesis within the shale, this organic matter turns to kerogen. It is the kerogen that is referred to when discussing organic matrix within the rock. This matrix can potentially make up a large portion of not just the total rock porosity, but also the total volume of the rock in general. 5% by weight total organic carbon shale, 10% of the shale volume is occupied by organic matter due to organic matter density of approximately ½ that of the inorganic matrix (Passey et al. 2010). Additionally, as much as 50% of the space occupied by the organic matter is open pore space. This means that approximately 20% of the total rock volume could be organic matrix. Through

SEM and TEM the pore sizes of this organic matrix have been shown to range from 5 to 1000 nm (Passey et al. 2010). In addition to this very fine pore space, the organic matrix is likely to have different properties of wettability as well as gas storability. The large internal surface area of the organic matrix allows for a large amount of adsorbed gas as well as a large amount of stored free gas in the internal volume.

The key dynamics to the development of carbon rich mudstone (shale) are that while shale appears rather homogenous it actually has a great deal of complexity in particle size and mineral type (Passey et al. 2010). Additionally, within a given shale system, there may be a great deal of vertical variability in Total Organic Carbon. This is due to the environment during which the shale was deposited. Having taken many thousands to millions of years to deposit, the separate layers often have many different characteristics. Maximum organic-carbon content occurs in the basal transgressive systems tract and decreases stepwise to background levels at the maximum-flooding downlap surface (Passey et al. 2010). In other words, large amounts of organic matter tend to accumulate at the transition zones of continental basins where neither open ocean currents nor land based water outflows would prevent their buildup.

Locating formations of interest requires not only knowledge of depositional environment, but also shale system kerogen types and maturity level. Due to their increased TOC, current targets for shale gas reservoir exploration are over mature oil-prone source rocks (Passey et al. 2010). Total organic carbon of the system is critical in the determination of suitability. Not only is TOC a good predictor of total porosity, it also is a good measure of gas saturation in the system. In addition to shale TOC, mineralogy plays an important role in shale system production. Shale systems vary widely in their mineral composition ranging from extremely quartz-rich in some parts of the Barnett, to largely carbonate in the Eagleford. The shale gas plays that contain greater than 50 wt.% quartz or carbonate tend to have a more brittle character that responds well to current well stimulation practices (Passey et al. 2010).

Kerogen (organic matrix) in the shale system is important and as much as 50% of the volume of in-situ kerogen could be pore space and presents a good location for free gas as well as adsorbed gas to reside in the system (Passey et al. 2010). He also speculates that water and hydrocarbons are stored and move by two entirely separate mechanisms. Because the kerogen surfaces are likely oil-wet they can contain adsorbed gas; however, because of this, water appears to be

stored within clay minerals in the system. With two separate storage mechanisms, water and gas flows appear to be independent of one another.

Finally, natural micro fractures make up the remainder of the pore volume. Several different ideas describe the role of micro fractures in shale in terms of both storability and hydrocarbon transmission. Some literature suggests micro fractures are a necessary condition to shale gas production and that without them, large scale connectivity would be impossible in the reservoir (Wang and Reed 2009). However, Passey contends instead that very few natural fractures exist, which has been shown in several SEM and TEM studies of thin section shale samples. This leads to two possible conclusions. The first is that any micro fractures in the shale system are induced; namely they are man-made. In this case, micro fractures cannot play a role in the storability of free gas in the system because they did not exist before the drilling process. On the other hand natural fractures could still be a necessary condition for large scale connectivity as they would act as conduits for fluid flow after the drilling process (Loucks 2012).

The case for a lack of in-situ natural micro-fractures is further bolstered by two important pieces of reservoir evidence. The first is a question of fluids migration. If indeed diagenesis did fracture the shale and create conduits for fluid flow, why do these shale systems still contain a great deal of hydrocarbons? With proper flow channels, it would be expected that the fluids would have moved to a conventional reservoir of greater porosity. Additionally, it is difficult to account for the over pressurized state of many shale reservoirs. Once again, with proper channels for fluid flow, it should be expected that pressure would deplete over time to be in equilibrium with the surrounding rock system. This has not been the state of shale systems to this point. It appears then that large scale connectivity cannot exist in situ in the shale system in light of this evidence. The question then becomes what is the scale of connectivity with a shale system?

PERCOLATION

While several methods are used to determine connectivity in complex systems, percolation theory has proven very effective at describing their global characteristics (Stauffer and Aharony 1994). The term “global characteristics” refers to the fact that every interaction of a system is not needed to understand the actions of the system as a whole. This theory, while common in the field of physics and materials science, has not frequently been applied to work in the hydrology or petroleum industries. What work has been done does not attempt to combine knowledge of

reservoir lithologies with that of percolation theory, but instead it is often a study of the nature of a particular, idealized system. Percolation theory at its basis is a system that describes the number and properties of nearest neighbor sites on a lattice (Stauffer and Aharony 1994). Individual lattice sites can then be either "on" or "off" with some associated probability for each. Percolation deals with the properties of nearest neighbor sites that are turned "on." The fundamental question answered by percolation is whether or not a system can communicate across its area or volume. Namely, imagine a glass cylinder filled with both insulating and conducting balls. Percolation theory answers the question what percentage of those balls need to be conductors so that an electric current flows from one side of the cylinder to the other. This example can be applied to any type of flowing systems where a portion of the space allows flow and another portion is closed off to flow.

More generally the percolation system does not require a lattice structure but instead can be randomly placed "porous" objects in a medium in what is termed continuum percolation. These systems tend to more closely mimic real physical systems as real systems rarely align themselves in perfect square or triangular grids (Ewing and Horton 2007).

A great deal of characterization of the percolating system deals with the area right around the first time at which a system percolates, or communicates across opposing faces. This is a critical property of the system and is referred to as the percolation threshold,P_c and it refers to the percentage of "on" sites in the system that is required to allow system percolation. If a lower percentage of sites are "on" then the system will not percolate. If a higher percentage are "on" then the system will continue to percolate with a larger share of lattice sites being intersected by the main, percolating cluster.

Additionally, questions regarding the average size of clusters below the percolation threshold can be answered. Knowing the geometry of a system and the average number of "on" sites is enough information to determine the average cluster size.

The first key concept in percolation theory is that macroscopic flow (electric current, volumetric water flow, hydraulic conductivity) is governed by a power law relationship of the form

$$Q\ \alpha\ (N - Nc)\text{^}k$$

where Q is the macroscopic flow rate, N the number of "on" segments in the system, Nc the number of "on" segments at the onset of percolation, and k the characteristic exponent of the system (Berkowitz and Balberg 1993). Additionally, they introduce the concept of universality whereby the solution for a simple problem allows for the solution of a more complex one. One of percolation theory's greatest advantages is that the characteristic exponent is the same for many different systems.

Several papers describe methods to apply the tenets of this model to hydraulic systems. For instance, a system was designed in both 2 and 3 dimensions to examine the relationship between local and global hydraulic conductivity (Berkowitz and Balberg 1992). Their system employed the continuum model by randomly placing conducting spheres (or circles in 2 dimensions) in an insulating volume. If any two spheres were found to overlap, the transmissibility between spheres was a function of the degree of that overlap. An overall hydraulic conductivity for the system could then be determined as a function of the number of spheres placed in the system. The results of these simulations could then be compared to theoretical predictions for continuum percolation.

The model described above employs a simplified porous media by using spheres of the same radius throughout the system. Additionally, there is no probability distribution associated with the placement of spheres as they are positioned randomly throughout the volume. Overlapping spheres are deemed to be communicating in the percolation system. Local conductivity is determined by the degree of overlap of the system, where the radius of the intersecting volume is the restriction on flow rate. Here, Hagan-Poiseuille flow is used to describe flow between adjoining spheres as pipe flow with the radius of the intersecting sphere region and length as the distance between two adjacent sphere centers (Berkowitz and Balberg 1992).

Spheres are then added to the system one by one and a check of percolation is conducted. OnceNc, the number of spheres in the system, reaches the percolation threshold a calculation of global hydraulic conductivity is made. This utilized Kirchhoff's law as the sum of the fluxes across each sphere must equal zero (Berkowitz and Balberg 1992).

The system required several assumptions which may cause deviation from real systems. The first is in regards to multiple overlapping spheres. Multiple overlaps are simply treated as separate

overlapping systems for ease of computation. Additionally, the cylindrical necks connecting individual spheres are treated as separate interacting components (Berkowitz and Balberg 1992).

Several conclusions are made from this study. The first is that the hydraulic conductivity of the system, K, follows a power-law dependence defined by

$$K\ \alpha\ (N/Nc - 1)\hat{}x$$

where N is that total number of spheres (or circles) in the domain, Nc is their concentration at the percolation threshold, and x is an exponent which depends on the dimensionality and the case (Berkowitz and Balberg 1992). From this, the critical exponent for hydraulic conductivity was experimentally determined. While the universal constant was determined for the 2 dimensional case as 1.2, the 3 dimensional case lacked a universal constant. The critical exponent was a function of how the spherical spaces interacted with each other.

There are two important characteristics to an experiment of this type. The first is that it is widely applicable to many types of porous media. Hence, by understanding the topology of a porous media, one can determine the critical exponent and properly characterize hydraulic transport properties. Unfortunately, because the critical exponent only provides proportionality between these features, it is difficult to determine hydraulic conductivity with greater precision than a single order of magnitude. The approximation may be too course for practical use (Berkowitz and Balberg 1992).

CHAPTER III

INITIAL APPROACH

MODEL THEORY

We begin by mimicking the approach of Berkowitz and Balberg (1992) by modeling the interaction of conducting spheres in space through a connection spherical pipe. Our model has several key distinctions from their model. First, for proof of concept of the model, we examine spherical units in 2 dimensions (i.e. an X by Y by 1 construction) as shown in Figure 3.1 below. Second, we align our spheres on a regular, square lattice in which distance between lattice sites can be prescribed. Third, we determine the exact degree of overlap between any two intersecting spheres. Finally, we attempt to measure permeability as a function of porosity as opposed to hydraulic conductivity in the case of Berkowitz and Balberg (1992).

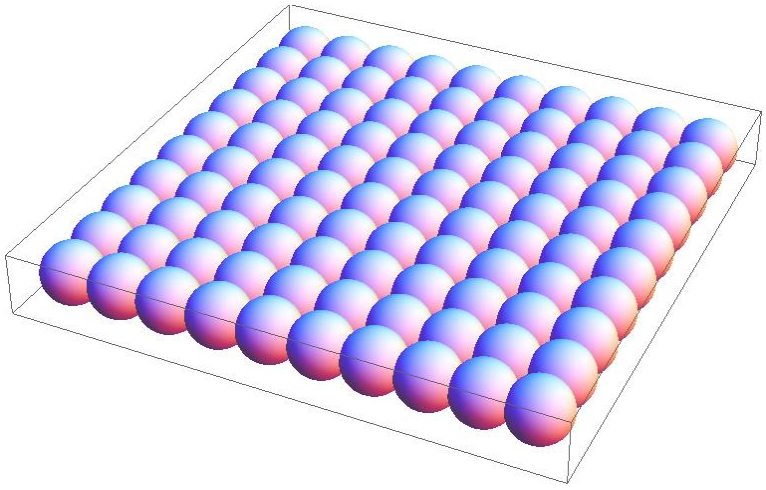

Fig. 3.1 – Model Example Showing Uniform, Overlapping Spheres

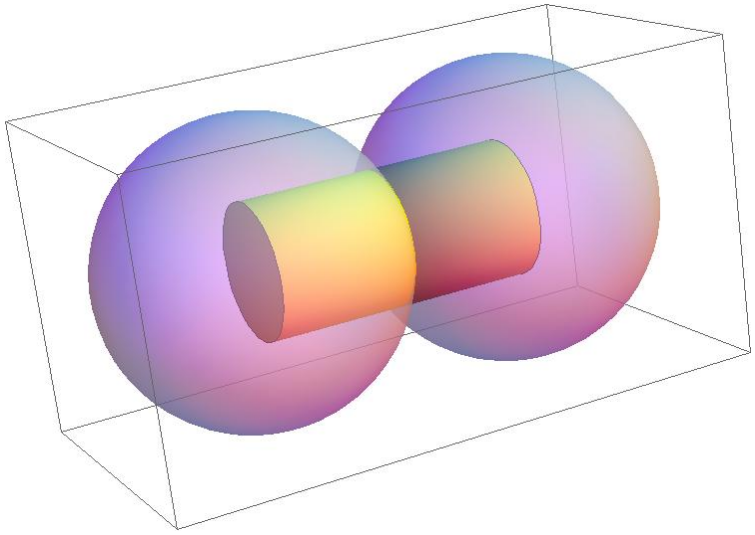

Fig. 3.2 - Pipe Flow Geometry Between Two Overlapping Spheres

The cross sectional area of the pipe is easily determined and given by:

$$Area = \pi * (\left(\frac{1}{2} * D\right)^2 * (4 * D^2 * R^2 - (D^2 - r^2 + R^2)^2))$$

$$D \text{ is the distance between sphere centers}$$

$$r \text{ is the little sphere center}$$

$$R \text{ is the large sphere center}$$

(Wolfram, 2012)

We look again at the 2D set of overlapping spheres and recognize that each set of overlapping spheres has the individual pore geometry show above in Figure 3.2. By using the basic Poiseuille equation governing pressure drop through a cylindrical pipe, we are able to construct a flow pattern through the system as shown in Figure 3.3 below.

$$\Delta P = \frac{8 * \mu * D * Q}{\pi * r^4}$$

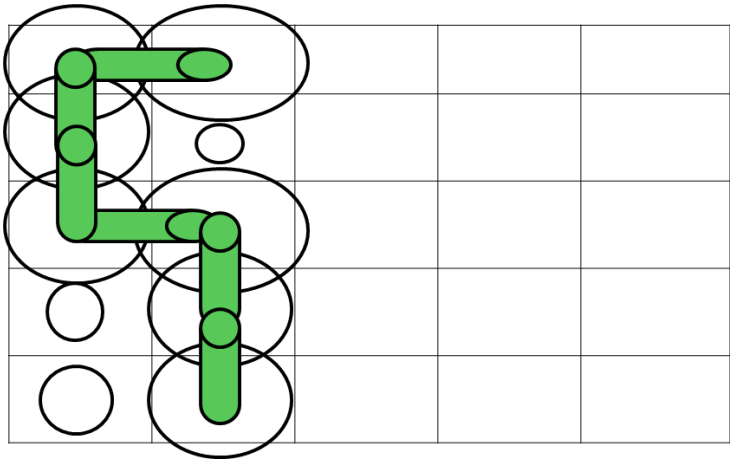

Fig. 3.3 - Path Connecting Pipes from Sphere to Sphere in the Larger Scale Model

If we assume a steady state condition for the system with constant pressure left hand and right hand boundaries as well as no flow boundaries on the top and bottom, we are able to determine both pressure and flow rate profiles for the system. Additionally, we are able to determine the porosity of the system.

2D LATTICE SIMULATIONS

Because system characteristics are intuitively understood, we begin with the simplest case where uniform sphere radii are used throughout the system. Radii are then increased incrementally from 0 to d/2 in order to show the variation of permeability with porosity. The system moves through the percolation threshold at exactly $r = (d/2)$ when adjacent spheres first touch. Above the percolation threshold we see the characteristic power law relationship $k = a * (P - Pc)\text{^}b$ as shown below in Figure 3.4.

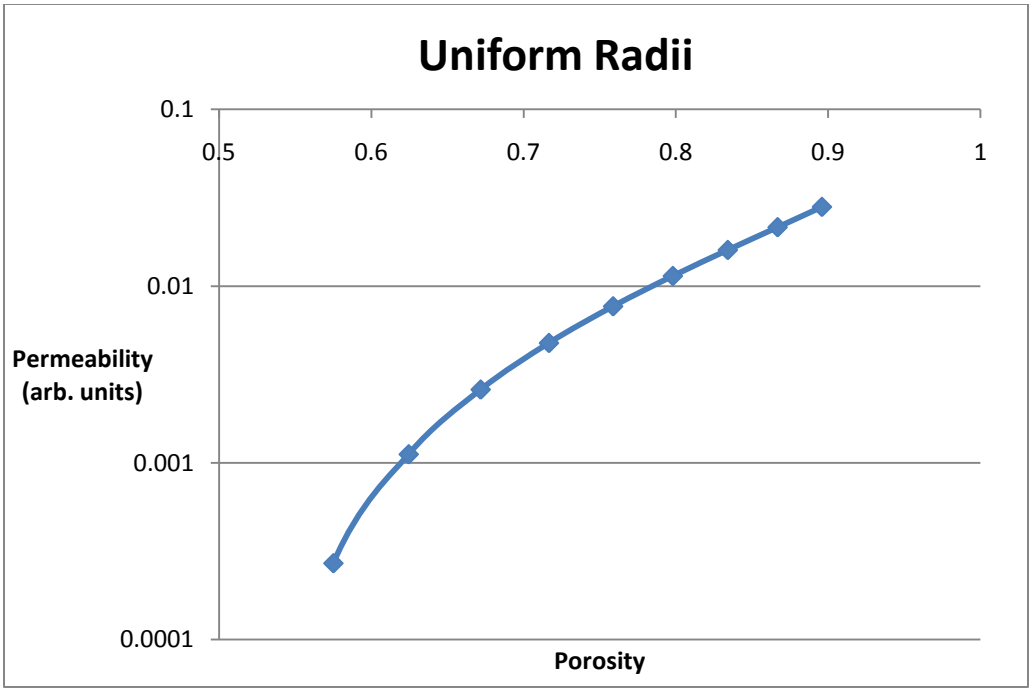

Fig. 3.4 – Uniform Radii semi-log Porosity-Permeability Profile

Additionally, we are able to characterize the system by determining the constants a and b in the power law equation, $k = a * (P - Pc)\text{^}b$. As shown below in Figure 3.5, regression analysis shows an exponent value of 2.3975 and a proportionality constant of 0.2564. This is consistent with the work of Berkowitz and Balberg who obtained exponent values of$2.3 \pm .1$.

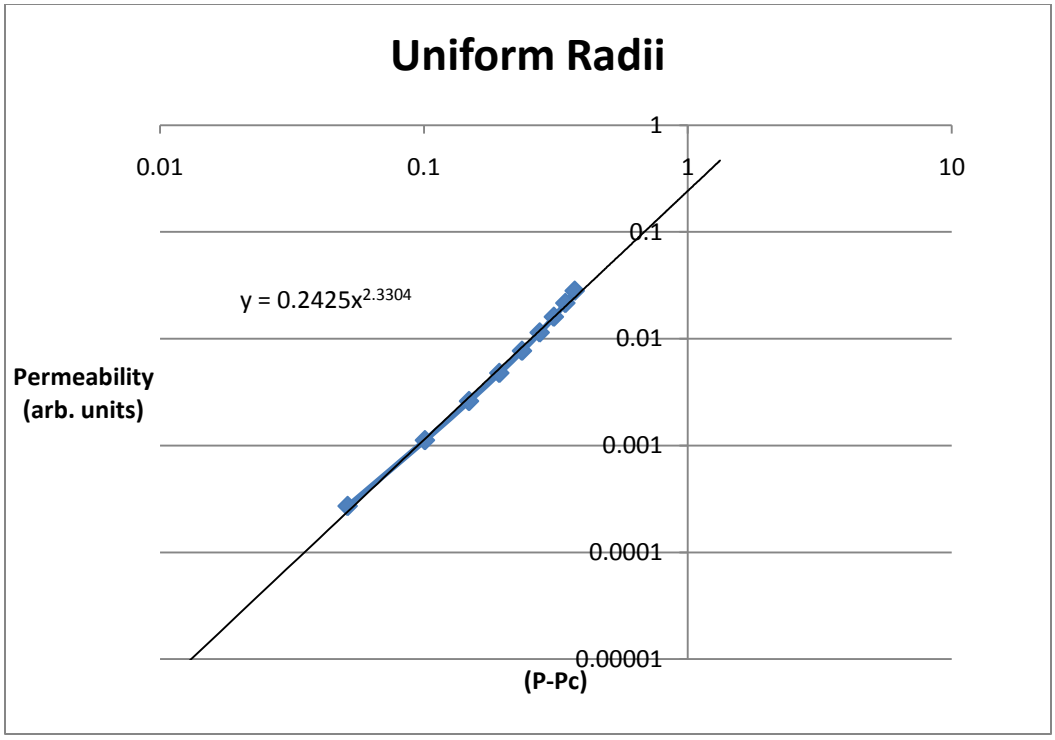

Fig. 3.5 – Uniform Radii log-log Percolation Threshold-Permeability Profile

We move next to the bimodal radii distribution case in which individual pore space at each node exists and has radius 1 or does not exist (has radius 0) with a range of probabilities from 0.4 to 1.0. We immediately see that this situation is tantamount to a regular 2 dimensional, square lattice percolation problem where adjacent "on" lattice points are able to communicate with one another. Once again we can see the characteristic power law behavior as shown below in Figure 3.6.

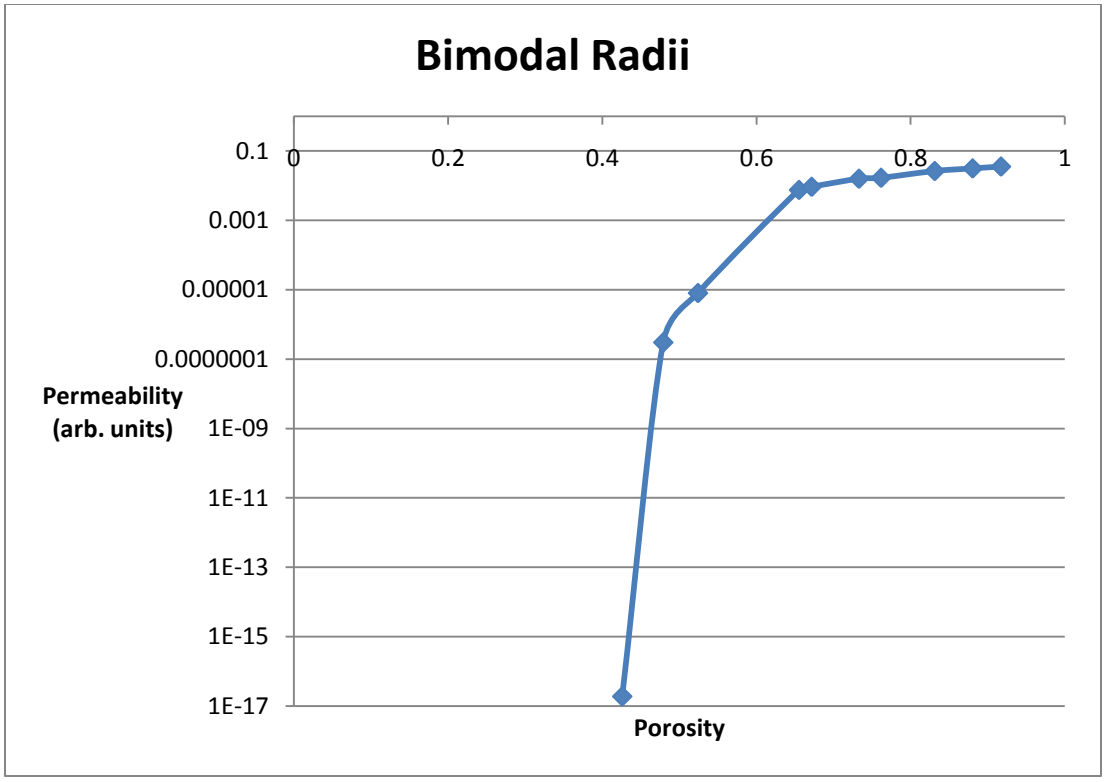

Fig. 3.6 – Bimodal Radii semi-log Porosity-Permeability Profile

The points in this data set are noisier than the previous problem because of an increased finite size effect. Because we are in the finite size realm it is possible to be above the percolation threshold even though the data suggests we are below the infinite lattice percolation threshold. The previous problem did not have the same finite effects because every lattice point was essentially on, with only a question of degree. In addition to porosity we also compare permeability to (P-Pc) as before to discover the characteristic constants as shown below in Figure 3.7.

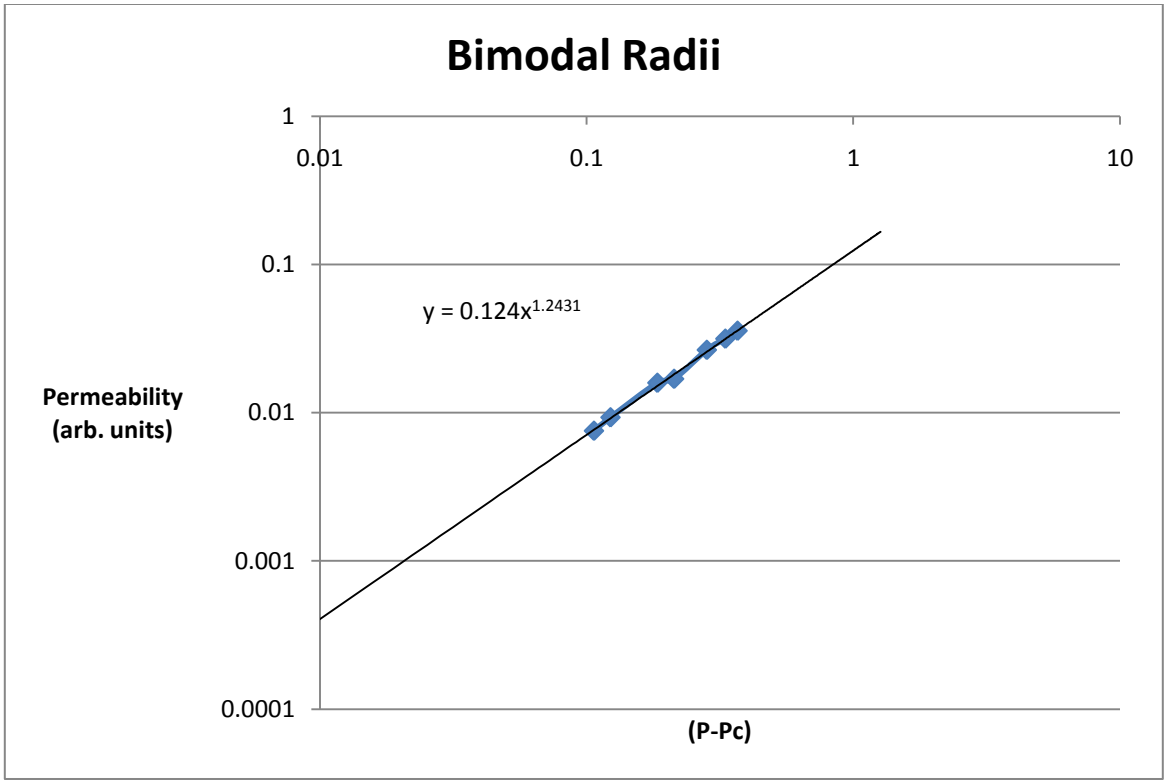

Fig. 3.7 – Bimodal Radii log-log Percolation Threshold-Permeability Profile

Once again we use $k = a * (P - Pc)^b$ to determine the shape of the equation and find $b = 1.2431$ and$a = 0.124$. This result agrees nicely with those of Berkowitz and Balberg (1992) which give a characteristic exponent of $1.2 \pm .1$. In this case, we also know the percolation threshold in the infinite lattice (as a percentage of occupied sites) to be Pc=0.5927 from the literature (Stauffer and Aharony, 1994) which equates to a percolation porosity of Pc=0.5485. This agrees roughly with the determined percolation porosity seen above of 0.45-0.50. Once again, finite size effects of the lattice can account for the small degree in variation.

We next attempt to mimic the true pore size distribution as observed by Elgmati et al. (2011). We are able to overlay a Rayleigh distribution to the sample pore size information from this distribution. In Figure 3.8 below we see a shifted Rayleigh distribution with standard deviation of 0.009 μm.

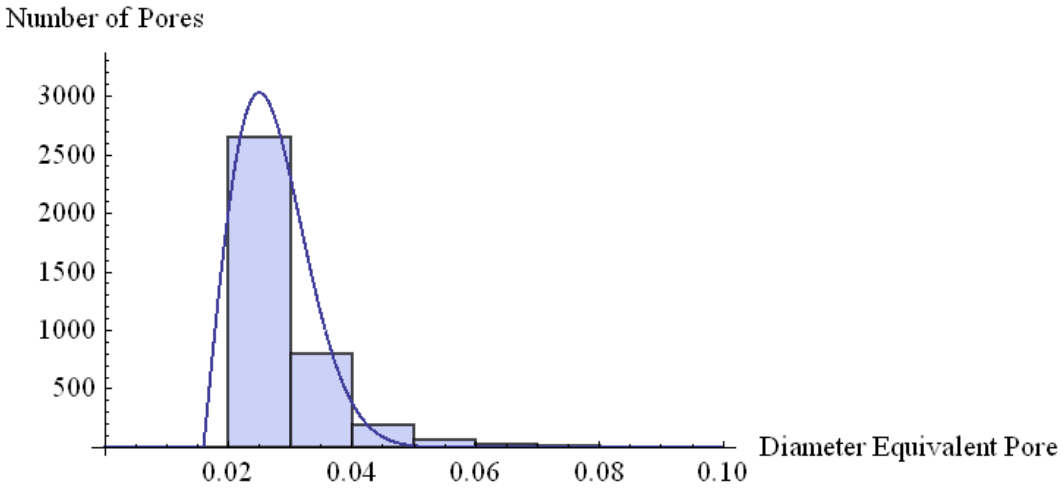

Fig. 3.8 – Rayleigh Distribution Overlain on a Pore Size Histogram (Elgmati et al. 2011)

225 data points are randomly sampled from this distribution and used to populate the model. Distance between cell centers plays a large role in the permeability of these systems (i.e. larger distances between cells results in lower numbers of inter cell connections and lower porosities). As a result, we start with the mean cell radius from the distribution above as the distance between cells and move to a distance of twice the mean. The Rayleigh distribution mean is calculated as $\sigma\sqrt{(\pi}/2)$ (Weisstein 2012). Because our system is shifted, this mean is increased by 0.016 μm to achieve better data fit. The graphs below (Fig. 3.9 and Fig. 3.10) show permeability as a function of both porosity and distance between cells. Once again we see the characteristic power law shape for permeability as a function of porosity.

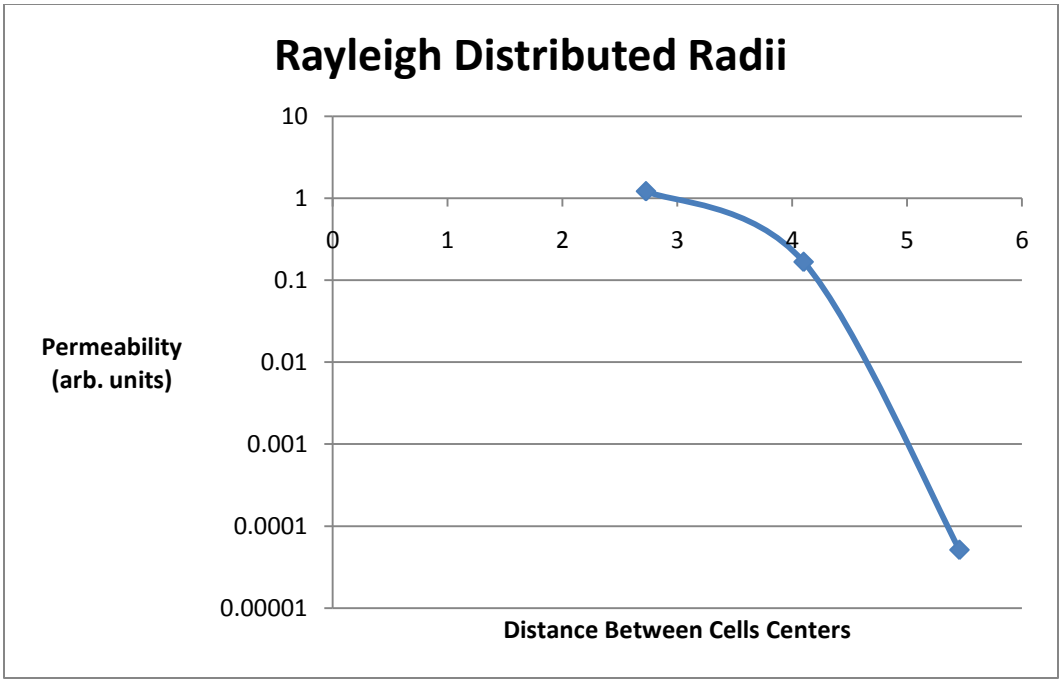

Fig. 3.9 – Rayleigh Distributed Radii Cell Distance – Permeability Profile

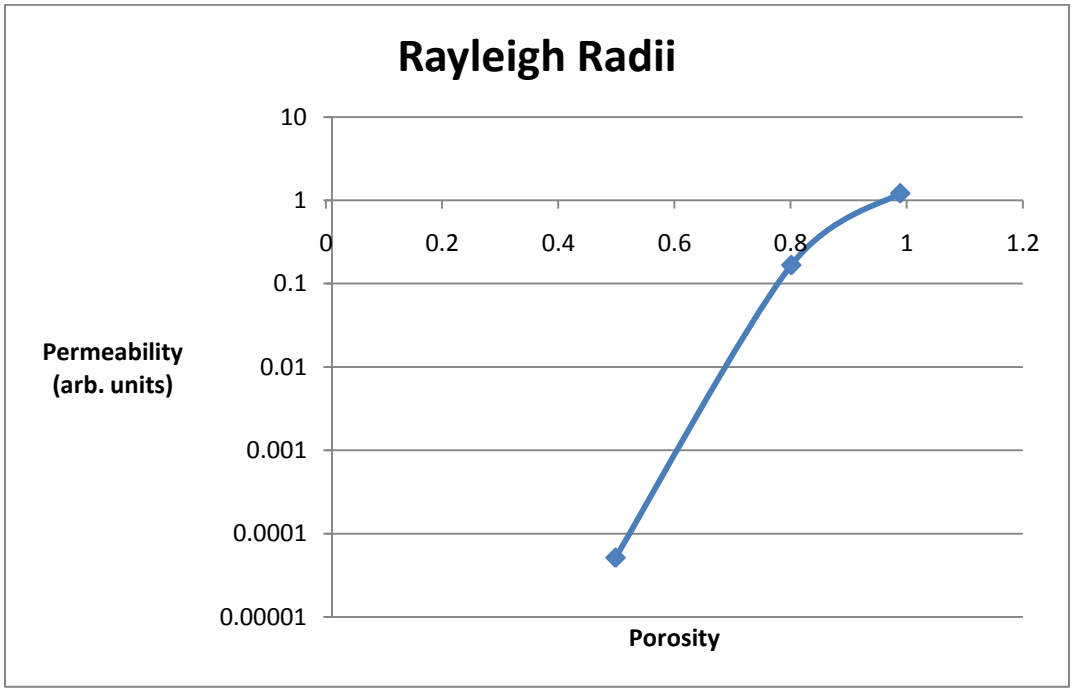

Fig. 3.10 – Rayleigh Distributed Radii Porosity– Permeability Profile

DISCUSSION OF RESULTS

We see from the results graphs above that permeability is indeed a function of porosity. However, because porosity is in a turn a function of the distance between cell centers, we are not able to solely rely on the pore size distribution as a determinant for system permeability. We also must know system porosity. In other words, in the case of the pore size distribution given above, we must also know the system porosity in order to determine whether or not the system has large scale percolation and subsequent permeability. Permeability drops sharply around 50% porosity implying a percolation threshold at approximately that point. In contrast to this, we note that in situ shale porosities in similar systems are on the order of 4%-8%. We see then that while pore size distribution in the model mimics that of the shale system, pore density does not. In order to fulfill both of these conditions, we fix the both the pore size distribution as well as pore density in order to determine permeability. For instance, increasing the distance between cell centers from 5.5 (as above) to 11 to accurately reflect the porosity of 7% leads to a permeability of 0 and recognition that we are below the percolation threshold.

This condition leads to several conclusions. First, because we know the shale system in question has large scale permeability and hence was above the percolation threshold, we know there must be inaccuracies in our model formulation. The first may occur as a result of the two dimensional nature of the model. The percolation threshold of a system is inversely related to its degrees of freedom. Hence, in a system such as described above, we are not accurately capturing the degrees of freedom in the system. Second, we may not be describing the pore geometry accurately. Higher aspect ratio and less uniform pore geometries tend to result in better connectivity. As the pore diameters used in our experiments were only equivalent pore diameters derived from non-uniform shapes, variation of pore shape may lead to more accurate results. The following sections describe solution to these problems.

CHAPTER IV

EXCLUDED VOLUME

THEORY

We look to the analytical technique of excluded volume to address some of the questions of pore geometry. Excluded volume is defined as "the volume around an object into which the center of another similar object is not allowed to enter if overlapping of the two objects is to be avoided" (Balberg et al. 1984). The simplest example is that of a sphere because we can neglect any orientation effects. Analytical techniques can be used to determine an object's excluded volume; however, these techniques require drawing the volume then averaging over angular distributions through which the object is rotated. Figure 4.1 below shows a sphere's excluded volume and the integration required to determine its average excluded volume based on orientation.

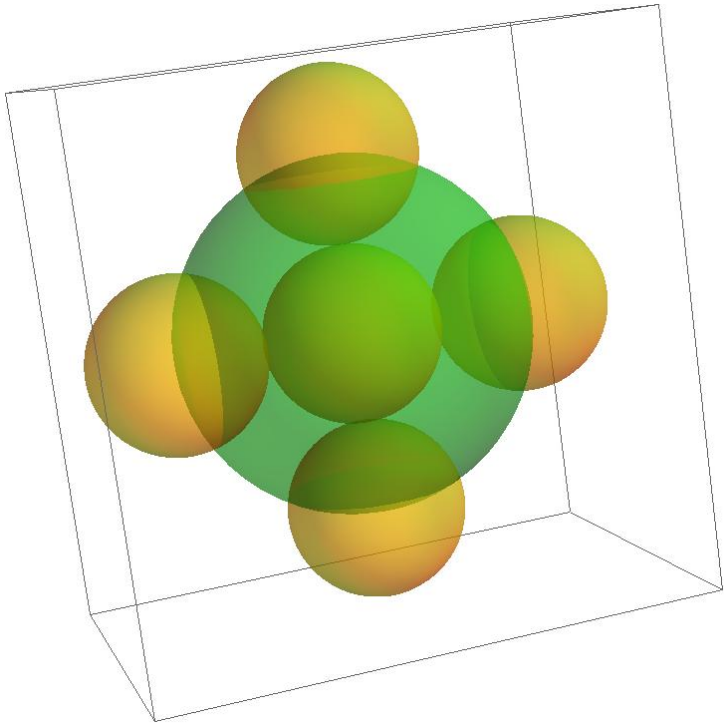

Fig. 4.1 – Excluded Volume Determination of a Sphere

The original sphere whose excluded volume we are attempting to quantify is centered inside the larger green sphere. In order to circumscribe the excluded volume, we move a sphere congruent

to the original, inner sphere around the surface of the original, inner sphere while tracing its center point. The path drawn by this method will trace the excluded volume of the original, inner sphere and is shown by the larger, green sphere. The excluded volume given for this example is:

$$vex = (4/3) * Pi * (2 * r)\text{^}3 = (32/3) * Pi * r\text{^}3$$

where vex is the excluded volume and r is the radius of the original, inner sphere. Integrating over the probability distribution for all orientations of the sphere $P(\theta,,\psi)$ yields

$$vex = \iiint \left(\frac{32}{3}\right) * Pi * r^3 \ P(\theta,,\psi) d\theta dd\psi.$$

Integrating over probability distribution, $P(\theta,,\psi) = 1$. This leaves $\left(\frac{32}{3}\right) * Pi * r^3 = vex$.

Hence, spherical pores have a v/vex ratio of

$$\frac{(4/3)*Pi*r\text{^}3}{(32/3)*Pi*r\text{^}3} = 1/8.$$

In order to obviate the cumbersome, manual process of drawing an excluded volume and integrating of angular probability distributions, it is far more common to use an analytical approach for convex objects or to use a Monte Carlo method in the case of non-convex objects (Saar and Manga 2002).

Saar and Manga (2002) present an equation for the determination of average excluded volume (average over all angular distributions) as

$$< vex > \approx Va + Vb + (AaRa + AbRb)/4\pi$$

where $< vex >$ is the average excluded volume, V is the volume, A is the area, and R is the mean radius of curvature for objects a and b (Saar and Manga 2002). For example, in the case of average excluded volume of a sphere normalized by the volume of the original sphere we have

$$\frac{v}{< vex >} = \frac{\frac{4}{3}\pi r^3 + \frac{4}{3}\pi r^3 + \frac{(4\pi r^2 * \mathrm{r} + 4\pi r^2 * \mathrm{r})}{4\pi}}{\frac{4}{3}\pi r^3} = 0.112 \approx 0.125$$

where all variables are as before.

In the case where convex objects are not under investigation or arbitrarily high precision is needed, Monte Carlo methods are used. This method places the two identical objects in a box with an arbitrary orientation and determines whether or not they intersect. The ratio of intersections to non-intersection times the area of the box will give the excluded volume (Saar and Manga 2002). Because our investigation is working under the assumption of convex object interactions (both spheres and ellipses) whose excluded volume is already well defined in the literature, we refer to previous works when determining their characteristics.

RELATION TO PERCOLATION POROSITY

The geometric idea of excluded volume is combined with the work of Balberg (1985) to determine percolation porosity. Balberg (1985) lays out a simple argument for determining percolation porosity as a function of the ratio of volume to excluded volume. He begins with a unit volume of insulating space as shown below in Figure 4.2. He then adds a conducting volume, v, to the space as shown below.

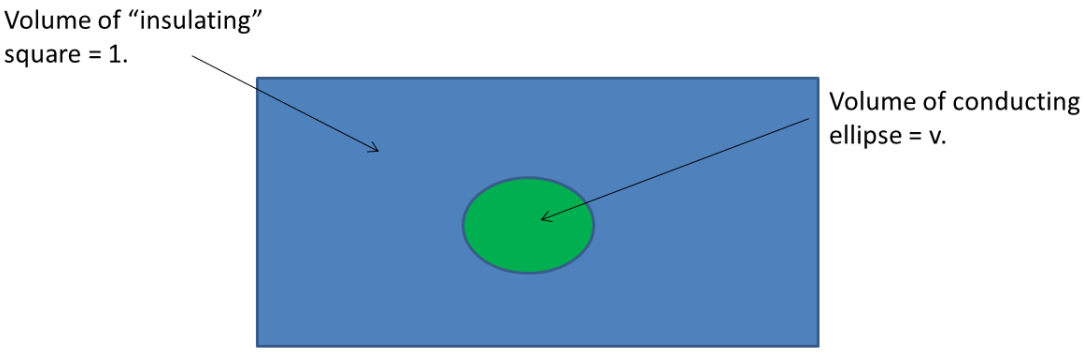

Fig. 4.2 – Basis for the Percolation Porosity by Excluded Volume Argument (Balberg 1986)

A random point in this space then has probability (1-v) of being in the impenetrable volume and v of being in the conducting space assuming the insulating space is of unit volume. At the percolation threshold we know that Nc total conducting volumes are in place and hence the probability of a random point not intersecting any of the conducting spheres is $(1-v)^{Nc}$. This probability is also related to the percolation porosity of the system by

$$1 - c = (1 - v)^{Nc}$$

We then substitute the identity $v = vex * Nc * v/(vex * Nc)$ in to the equation, which yields

$$c = 1 - \left[1 - \left(Nc * vex * \frac{v}{vex}\right) * \left(\frac{1}{Nc}\right)\right]^{Nc}.$$

In the infinite limit where $v \to 0$ and $Nc \to \infty$, the equation is of the form

$$c = 1 - e^{-\left(c * \frac{v}{vex}\right)}$$

where $c = Nc * vex$, which is constant for a particular system. C is determined experimentally, but has been shown to be of order 1. For instance, in the case of spherical pores c=2.8 and v/vex=8 as shown above yields a percolation porosity, $c = 1 - e^{-\left(\frac{2.8}{8}\right)} = 0.29$.

We see from the above equations that the v/vex ratio largely determines the percolation porosity of the system. In fact, the Taylor series approximation of

$$c = 1 - e^{-\left(c * \frac{v}{vex}\right)} \approx \frac{c * v}{vex} \approx \frac{v}{vex}$$ (Wesstein 2012).

As a result, the percolation porosity can be an arbitrary value for any $\frac{v}{vex}$ ratio . For example, shapes with large excluded volumes relative to their original volume begin to have vanishingly small percolation porosities. This situation occurs with shapes of large aspect ratios. For instance, elongated channels have a volume $v = \pi * r^2 * L$ and excluded volume $vex = \pi * r * L^2$. With $c = c * \frac{r}{L}$, we see that the percolation porosity can be made arbitrarily small based on the aspect ratio $\frac{r}{L}$, of the elongated channels. The graph below (Fig. 4.3) shows that percolation porosity approaches zero for smaller and smaller aspect ratios of v/vex. The envelope represented by the region in blue represents the various likely c values for different shapes and realizations and ranges from c=1 to c=3.

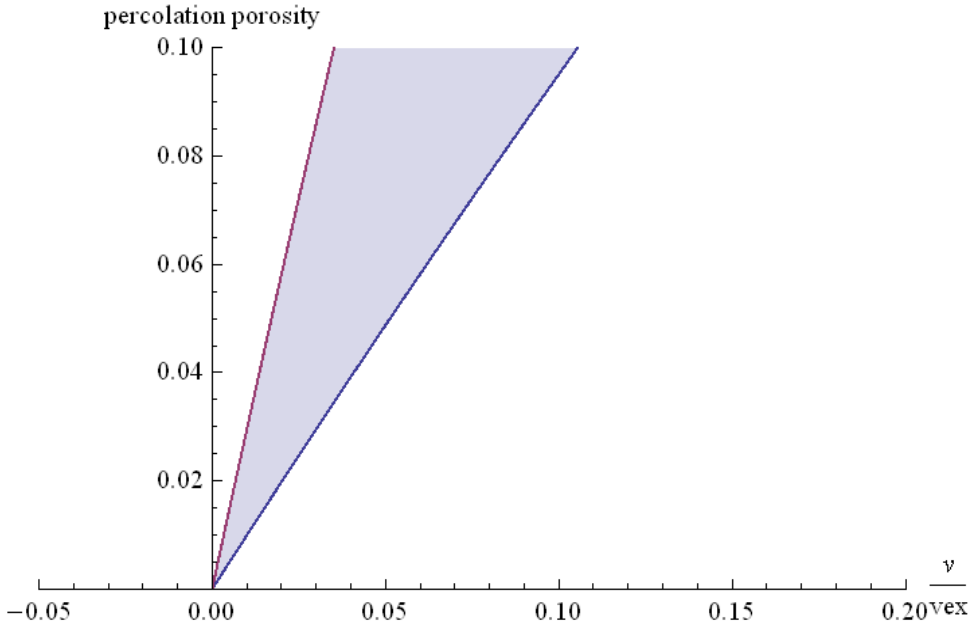

Fig. 4.3-Percolation Porosity as a Function of v/vex Ratio

For example, we see that if a shape under inspection had a $\frac{v}{vex}$ ratio of $\frac{1}{25}$ then the percolation porosity would range between 0.035 and 0.100 depending on the constant c which is a function of the system in question. Additionally, in the event that objects in the system are not the same size, we look at their average properties to determine the percolation porosity. Hence, for the spherical system examined earlier, $v = \left(\frac{4}{3}\right) * \pi * < r >^3$ and $vex = \left(\frac{4}{3}\right) * \pi * 8 * < r >^3$, where <> denotes average radius length. In the case of the Rayleigh distribution observed in earlier shale sample (Initial Approach, Simulation Results), we know the average radius length is $< r >= \sigma\sqrt{\frac{\pi}{2}}$, and hence see that the v/vex is invariant with radial distribution. Additionally, Balberg et al. (1984) showed c to be constant under various pore size distributions. This shows that regardless of pore size distribution, percolation porosity is invariant in the spherical pore case.

Additionally, because the porosity of shale reservoirs is frequently between 4%-8%, we know that the spherical pore description must be inaccurate. As was determined earlier, large scale permeability does not occur until 29% porosity regardless of pore size distribution. Therefore,

we must look to higher aspect ratio pore geometries with percolation porosity in the 5% region in order to explain large scale connectivity in the shale system.

Work on percolation of soft core prisms indicates percolation porosity is related to shape anisotropy (Saar and Manga 2002). We can see in the graph below (Fig. 4.4) that as the aspect ratio (semi minor/semi major axes)[1] of the ellipsoids increases in either direction, the percolation porosity decreases. The peak percolation porosity reaches a maximum for sphere at 29% as shown at the top of the graph.

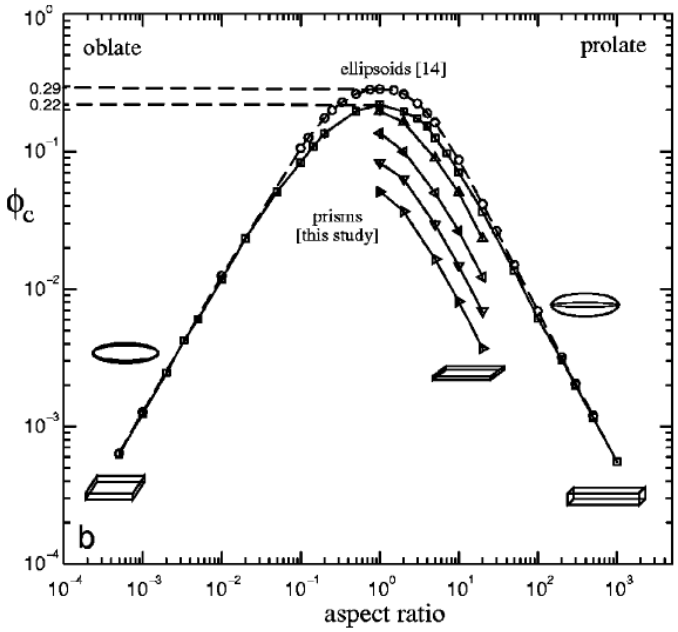

Fig. 4.4- Percolation Porosity as a Function of Pore Shape Aspect Ratio (Saar and Manga 2002)

Using the formula for normalized excluded volume given by Saar and Manga (2002), we can determine the percolation porosity for an ellipsoid of any aspect ratio.

$$\langle \overline{v_{ex}} \rangle = \langle v_{ex} \rangle / V$$

[1] Because an ellipsoid is 3 dimensional, 2 axes do not determine its extent. In the case of oblate ellipsoids, two of the axes are of the larger dimension and 1 is smaller. In the case of prolate ellipsoids, two of the axes are the smaller dimension and 1 is larger. The aspect ratio simply refers to large axis over small axis. See Figure 4.4 for visual representation.

$$\langle \overline{v_{ex}} \rangle_e = 2 + \frac{3}{2}\left(1 + \frac{\sin^{-1}\epsilon}{\epsilon\sqrt{1-\epsilon^2}}\right)\left(1 + \frac{1-\epsilon^2}{2\epsilon}\ln\frac{1+\epsilon}{1-\epsilon}\right),$$

$$\text{Where } \epsilon = \left(1 - \left(\frac{b}{a}\right)^2\right)^{.5}$$

With a, the long and b, the short axis respectively

From previous derivations, $c = 1 - e^{-\left(c*\frac{v}{vex}\right)}$, substituting in for v/vex as given above and assuming a c value between 1 and 3, we can make an estimation of percolation porosity. For instance, for an oblate ellipsoid where the major axis is 10 times the length of the minor axis, using the formula above we find the normalized excluded volume equals 26.38. Substituting this into our formula for c we have yields $c = 1 - e^{-\left(2*\left(\frac{1}{26.38}\right)\right.} = .073$ or 7.3% porosity. Additionally, Saar and Manga note the linear relationship between c and shape anisotropy at extreme (10^{-2}) levels of anisotropy

$$\phi_c = \begin{cases} 0.6/\xi & (\text{prolate}) \\ 1.27/\xi & (\text{oblate}) \end{cases}$$

where ξ is the shape anisotropy (larger side divided by the smaller side). This allows for the determination of c based solely on shape anisotropy. Hence, if a shale core sample has large scale connectivity and is only 1% porous, then the shale pore shape must have on average at least

$$0.01 = \frac{0.6}{\xi}$$

$$\xi = 0.6/0.01 = 60$$

times greater length of the semi major than the semi minor axis. Remember that the linear relationship holds true only in the case of extreme shape anisotropy and hence cannot be applied at levels lower than ≈50.

CONCLUSIONS

We finish the section on excluded volume by once again relating it to our knowledge of shale geology and discussing conclusions that can be drawn from those facts. First, we saw for a shale system with uniform pores that have an aspect ratio of 10 we can achieve large scale connectivity at only 7.3% porosity, which is within the porosity range of shale systems. Qualitative investigation of shale SEM and TEM images suggests that in general, pore shapes have an aspect ratio less than 10 for inorganic matrix, and certainly less than 10 in organic matrix, which generally has spherical pores. How then is large scale connectivity achieved in these systems? The ideas of excluded volume tell us that the onset of percolation is controlled by the highest aspect ratio objects in the system. Hence if a percolating system whose constituent objects have aspect ratios of 1000 is superimposed on a non-percolating system with aspect ratio 10, the result is a percolating system with a much larger connected volume.

Imagine percolating system 1 has constituent pore aspect ratios of 1000 and hence a percolation porosity of 0.6/1000=0.06%. Additionally, non-percolating system 2 has constituent pore aspect ratios of 10 and hence a percolation porosity of 7.3%. These two systems are then superimposed. The resulting system will continue to percolate as large scale connectivity is controlled by the high aspect ratio pores. However, the resulting system will be roughly 7.36% porous and have much higher levels of reachable pore space on the order of 5%. While we leave an analytical determination of connected pore space in dual porosity systems to later work, we note the analogy of this system to fracture networks in shale systems. It is the fracture network (high aspect ratio pores) that determine permeability while the high volume pores (low aspect ratio) determines fluids in place.

While these tools are critical for describing features of the shale system including percolation porosity, they still are not able to analytically determine permeability at and directly above the percolation threshold. For that we must move to continuum percolation simulations.

CHAPTER V

CONTINUUM MODEL

MODEL THEORY

We begin the development of the continuum model in 3 dimensions in much the same way the lattice model was constructed. First, we have an impermeable medium into which permeable spheres are placed. We then ask the question if any spheres intersect the left boundary of the system. If a sphere does intersect the left boundary, we determine if that sphere then intersects any other spheres. The system is then built out by connecting additional spheres that were in contact with the original. Finally we determine if any of the spheres in this set intersect the right boundary. If so, we are able to determine the percolation set (the set of spheres that constitute the percolation cluster). The image below (Fig. 5.1) shows a percolation cluster in blue and unconnected pore space in red. In this example, 50 spheres were randomly added to a 10X10X10 box all with equal radii of 1.3. The cluster must span the x direction from -5 to 5 to allow for the onset of percolation.

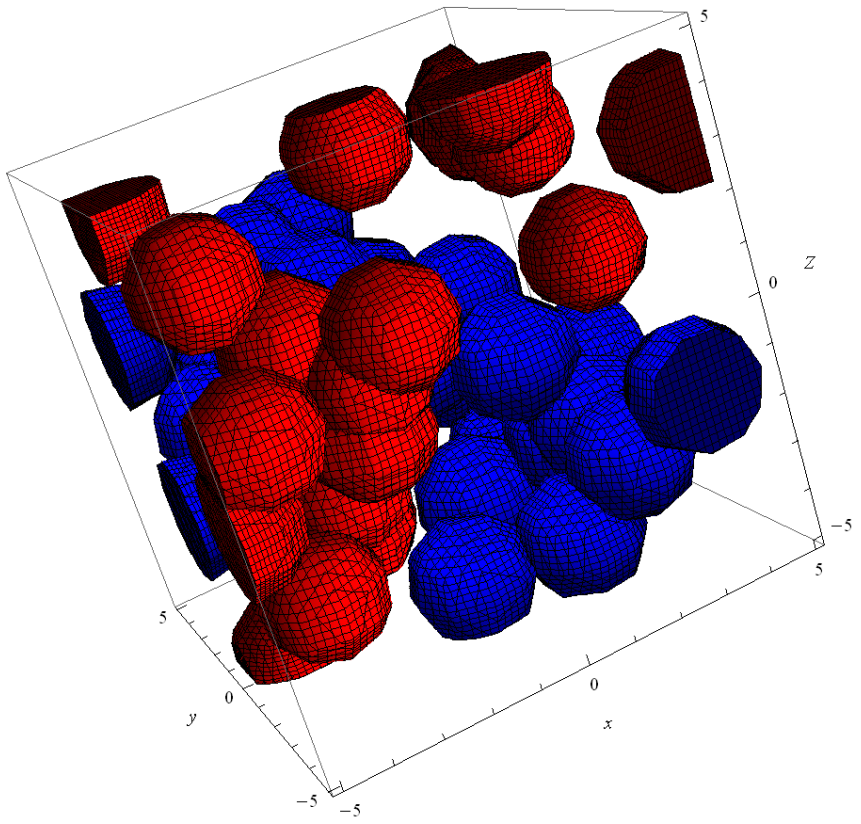

Fig. 5.1 – A 50 Sphere System with the Percolation Cluster Shown in Blue

Additionally, we can determine the porosity of the system with Monte Carlo methods. A point is randomly placed in the system and then it is determined if this point intersects any of the permeable spheres. The test is repeated 10^5 times where the number of intersects divided by the number of total randomly placed points is equal to the system porosity. The example shown above has a porosity of approximately 31.88%. Additionally, we are able to determine the percentage of pore space invaded by the percolation cluster. With a similar Monte Carlo argument as given above, we insert a random point into the box then determine if it intersects the percolating cluster, the non-percolating spheres or neither. The ratio of those points intersecting the percolating cluster to those intersecting the non-percolating cluster gives us the percentage of pore space invaded. This test is conducted 10^5 times for accuracy and determined that 60.24% of the pore space was invaded in the example shown above.

We continue the construction of our 3D model with the development of a pressure solver for the continuum case. This method mimics that of our on-lattice model (we refer to Appendix A for model basics) with the exception of the development of transmissibility. Instead of an exact transmissibility derivation as was done previously, we use the method presented in Berkowitz and Balberg (1991) as shown below (Fig. 5.2). In their description of transmissibility, they determine the overlap between any two spheres as a distance

$$\in = (2 * r - d)$$

where r is the radius of each sphere and d is the distance between sphere centers. Additionally, from previous derivations of Poiseuille flow, we see that hydraulic conductivity is proportional to

$$k \propto \frac{\pi * r^4}{8 * \mu * L} \propto \frac{A^2}{L} \propto \frac{r^{2*(d-1)}}{L}$$

where d is the dimension of the system.

Substitution of $r = (a * \in)^{1/2}$ and L =$2 * (a * \in)^{1/2}$ yields,

$$k \propto \frac{(a * \in)^{\frac{1}{2}^{2*(3-1)}}}{2 * (a * \in)^{\frac{1}{2}}} \propto \frac{(a * \in)^{\frac{4}{2}}}{(a * \in)^{\frac{1}{2}}} \propto (\in)^{\frac{3}{2}}$$

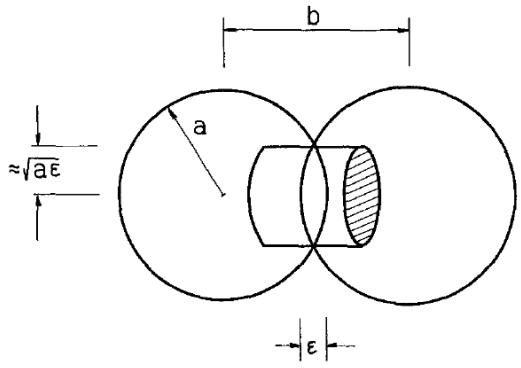

Fig. 5.2 – Overlapping Spheres Explanation of Pipe Flow (Berkowitz and Balberg 1992)

Because we are attempting to determine permeability as opposed to hydraulic conductivity, we factor μ out of the equation by setting it equal to 1. With this new basis, the transmissibility between any two spheres is simply determined by

$$T = (r1 + r2 - d)^{1.5}.$$

In addition to sphere-sphere transmissibility, we must also determine transmissibility between spheres and systems boundaries. These are found in much the same manner as the sphere-sphere interactions. The system boundary is assumed to be the midpoint between two identical intersecting spheres. Hence, the distance between the center point of the sphere and the system boundary is assumed to be $d/2$. Once again $\in= (2 * r - d)$ applies, where r is the radius of the intersecting sphere.

Additionally, we note the inherent limitation of this method is that no two spheres can exactly overlap nor can a sphere center lie exactly on the system boundary because the transmissibility calculation breaks down at $d = 0$. This is very unlikely in the case of randomly placed spheres; however, the possibility does exist for extremely large systems and is noted as such.

Knowing the transmissibility between any two spheres allows us to determine the system wide pressure profile and subsequent flow rates. In addition to the Gauss-Seidel iterative scheme for determining pressures, we employ a direct method to increase computing time in the case that the transmissibility matrix in nonsingular. As in the lattice case, we are able to determine a macroscopic permeability for the system. We can then compare porosity and permeability to make a determination of percolation porosity as well as the characteristic power law exponents we saw in the lattice case. Additionally, we are able to compare analytical solutions to the percolation problem with the simulation results.

CONTINUUM SIMULATIONS

We begin with a simple percolating example to test code efficacy and display system features. In the figure below (Fig. 5.3), we see an aligned set of 11 spheres that represent a percolating cluster. The pressure at the left face $(x = -5)$ is held constant at 100 while the pressure at the right face $(x = 5)$ is held constant at 0. The pressure drop along the aligned spheres is visible in the figure below.

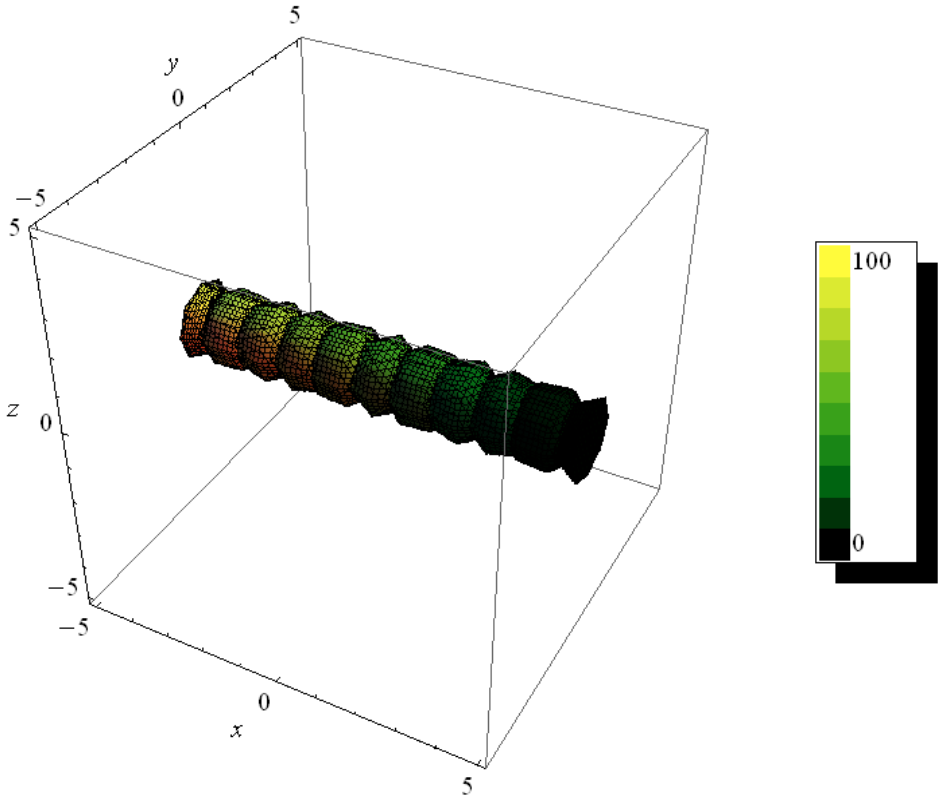

Fig. 5.3 - Pressure Solution Along a Straight, Percolating Cluster

Additionally, we see the numerical values of the pressure profile in Figure 5.4 below. As is expected, there is a straight line pressure decrease from system boundaries through each sphere center.

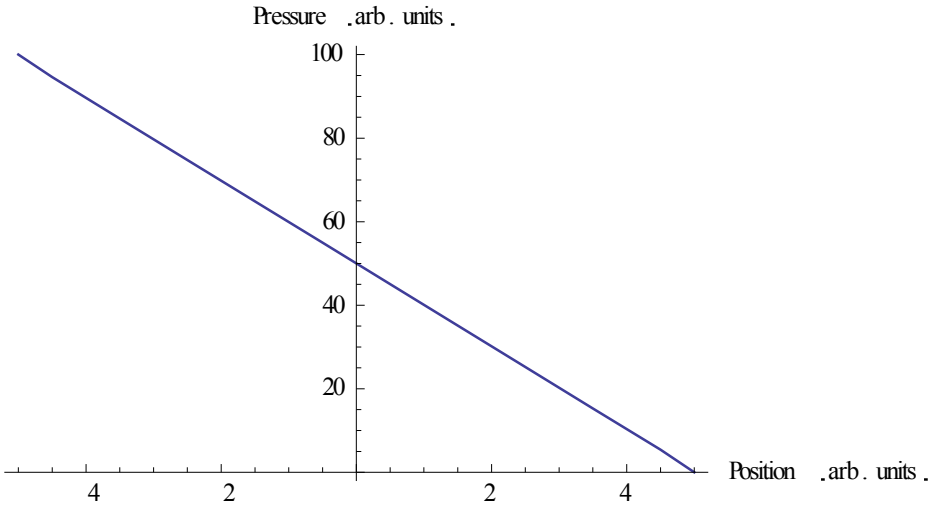

Fig. 5.4 – Straight Line Pressure Profile for Horizontally Aligned Spheres

We are also able to view the flow rate for each sphere. Flow rate is calculated as the transmissibility times the pressure drop between any adjoining pair of spheres. Flow rate is built in matrix form where the i, j^{th} entry shows the flow rate from sphere i to sphere$j$. Flow into each sphere is negative where flow out of each sphere is positive. Figure 5.5 below shows the flow rate profile for the pressure profile shown above.

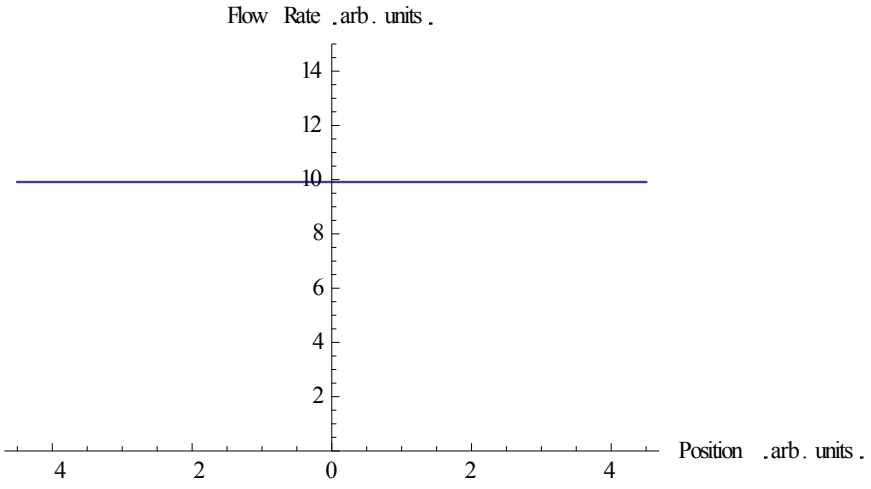

Fig. 5.5 – Constant Flow Profile for Horizontally Aligned Spheres

In the case of larger systems, total flow rate is calculated as the sum of flow across the left or right system boundary. The left boundary will show flow rates as negative, or into the boundary cells. The right boundary will show flow rate as positive, or out of the boundary cells. Left and right boundary flows must them sum to zero to show conservation of mass in the system. Because only one sphere intersects each of the left and right boundaries in the system shown above, the boundary flow calculation is trivial. However, we see that the flow rate is equal to -9.912 on the left face and 9.912 on the right, which is the same for all constituent cells in the system (as shown in the graph above). These two values sum to zero showing conservation of mass and system consistency.

In order to determine system permeability, we simply apply Darcy's Law to the macroscopic system. With Darcy's Law given below as

$$Q = \frac{kA}{\mu} * (\frac{dp}{dl})$$

where k is the system permeability, A is the area normal to the out system boundary, μ the fluid viscosity and $(\frac{dp}{dl})$ the pressure drop per unit length. We rearrange the equation to solve for k where, for the system example above, Q = 9.912, $A = 100$, μ = 1, and $\frac{dp}{dl} = \frac{100}{10} = 10$. As a result

$$k = \frac{\mu Q}{A} * \frac{1}{\frac{dp}{dl}} = 0.009 \text{ arb. units.}$$

Permeability is left in arbitrary units and is useful for comparison purposes only at this point; however, it is a simple process to make an estimate in field units for system permeability as well. For the example, assuming a viscosity of μ =0.0244 cp, calculating the area normal to the outer boundary $A = 2.73 * 10^{-10}\ ft^2$, and $dp = 1$ psi, $dl = 10 * 10^{-6}$ ft, and $Q = 9.9 * 10^{-8}$ stb/d we find that $k = 786.92\ md$. While this value appears high, it is consistent with the straight "pipe-like" geometry of the system (Darcy's Law and Applications 2012).

We next examine a system similar to that of Figure 5.1. Once again, we place 50 spheres into a 10X10X10 cubic region and demonstrate the percolation cluster pressure drop as shown in Figure 5.6 below.

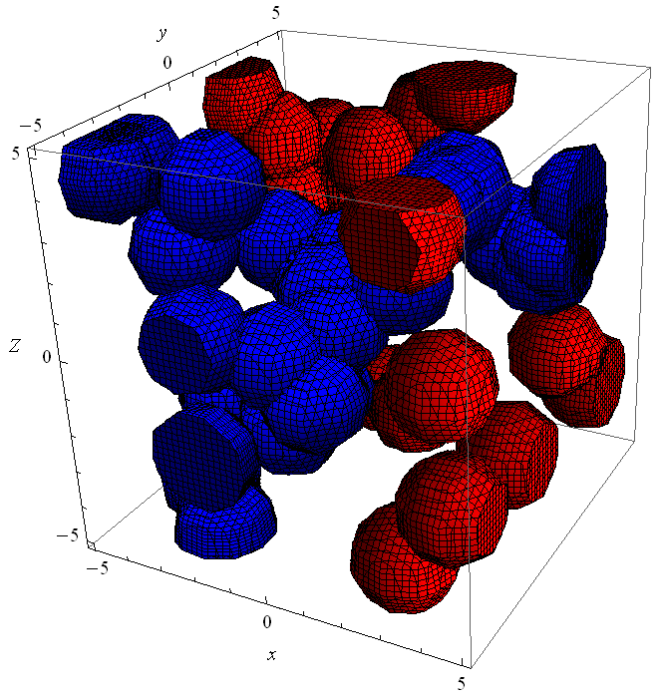

Fig. 5.6 – A Percolating Cluster Shown in Blue with a 50 Sphere Realization

The same method used to calculate pressure drop in the horizontally aligned system above is also used in the 50 sphere realization. We can see in Figure 5.7 below that those spheres intersecting the left boundary have a yellow hue and represent the high pressure region. As the system moves to the right boundary, we see the pressure drop to zero. Small transmissibility between adjacent cells represents choke points or poor connectivity and manifests itself as large pressure drops represented by large color variations in the figure below.

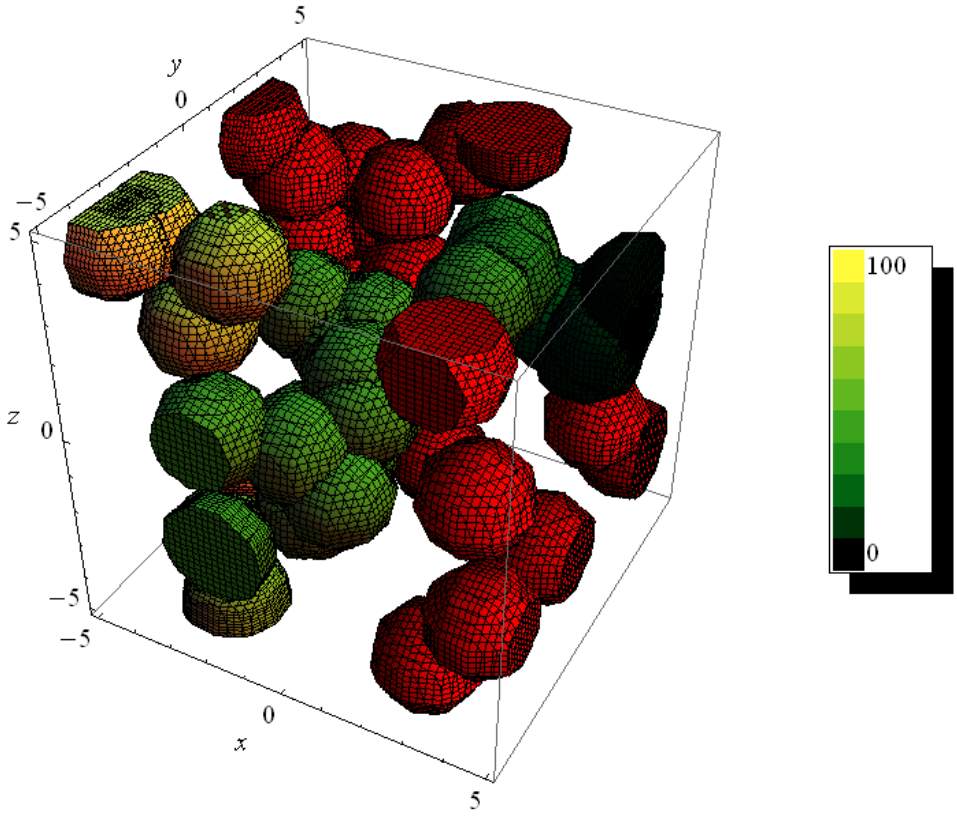

Fig. 5.7- Pressure Profile of the Percolation Cluster Shown in Figure 5.6

LARGE NUMBER SIMULATIONS

We now examine structures with large numbers of spheres in an attempt to mimic the porosity-permeability profile for the infinite spherical system. We initially look at 1500 permeable spheres placed into the same 10X10X10 impermeable region as was done in the example above. Starting at uniform radii of 0.15, the radii are increased incrementally in steps of 0.025. These values allow the system to start below the percolation threshold and then to move through it with a reasonable number of radial size increases. In general, studies aim to determine Nc, the critical number of spheres necessary for the onset of percolation (Berkowitz and Balberg 1992); however, our study is concerned with mimicking the radial distributions of pores seen in actual shale systems. As a result, we must vary the spherical radii in order to determine system properties.

The initial results for the 1500 sphere system are presented below (Fig. 5.8). Unfortunately, due to finite size effects, there is a large distribution in permeability as the system moves through the

percolation threshold. In fact, the percolation threshold is not at all easily determined from the graph below.

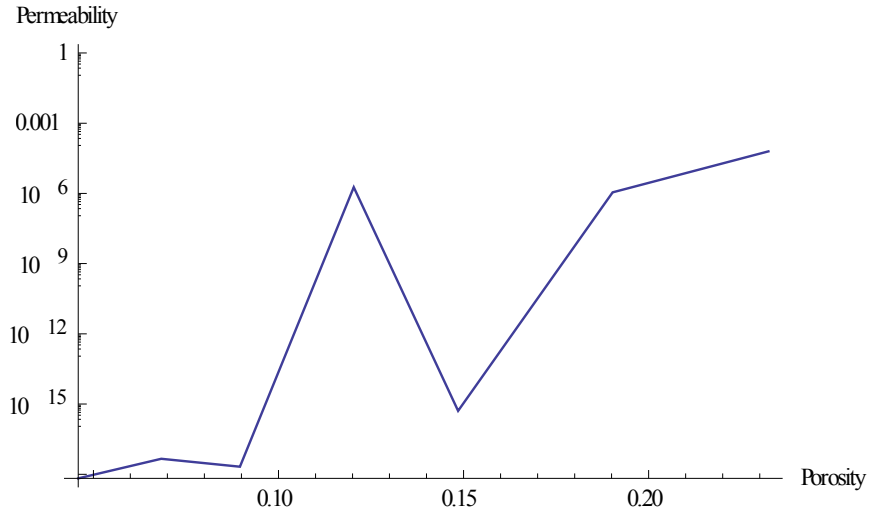

Fig. 5.8 - Porosity - Permeability Chart Showing Results of Finite Size Effects

To account for finite size effects, we must run a series of simulations to determine the percolation porosity. Porosity in this case was once again determined by Monte Carlo methods as was explained in section 1 of this chapter. The figures below (Fig. 5.9 and Fig. 5.10) show comparable systems to the one above. In this case, 6 different realizations for the same porosity were conducted below and above the percolation threshold to give a total of 24 different realizations. We begin to see the convergence of permeability at different porosity levels and a clearer picture of where the percolation threshold is for the spherical system.

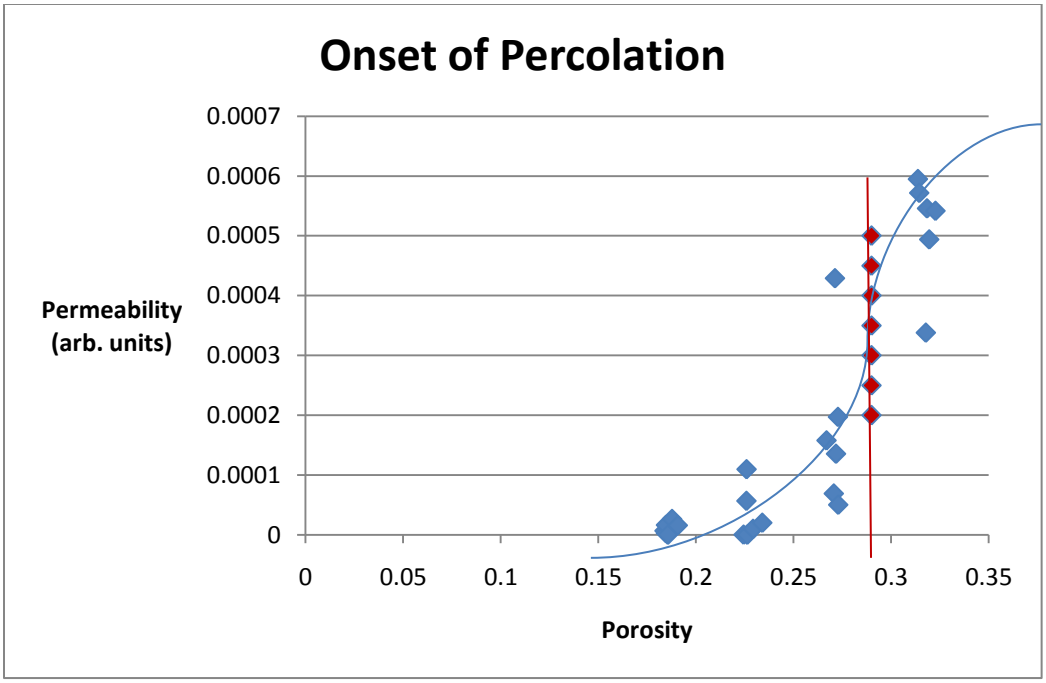

Fig. 5.9 – Blue Points are Experimentally Derived. Red Points Represent the Analytically Determined Percolation Threshold Porosity of 29%

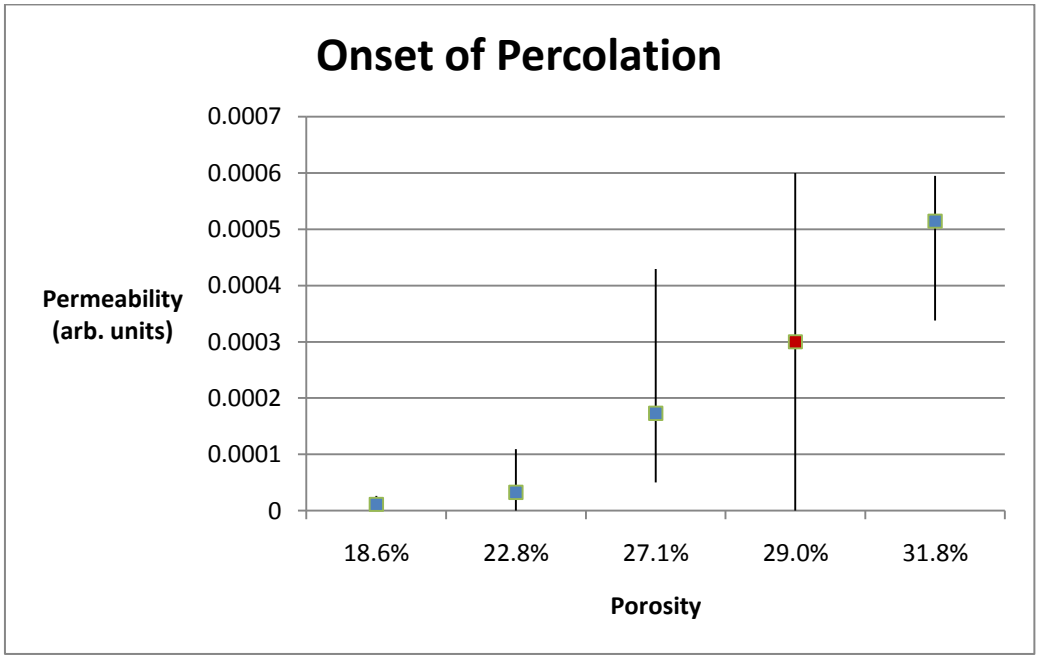

Fig. 5.10 – The Minimum, Maximum, and Mean of Experimentally Derived (Blue). Analytically Determined (Red) Permeability

As is expected in the finite size case, we have a blending, as opposed to a sharp front at the percolation threshold. As the size of the system approaches infinity, the percolation front becomes sharper and sharper. This fact is displayed in the figure below where the probability of percolation is used as a proxy for permeability. We can see that for the finite size case, there is a reasonable expectation that there will be large scale connectivity in the system even when we are below the percolation porosity threshold in the infinite case. While the systems they represent are different and hence so are the percolation porosities, we see that the shape of our interpolated permeability profile in Figure. 5.9 above closely resembles that in Figure 5.11 below around the known percolation threshold.

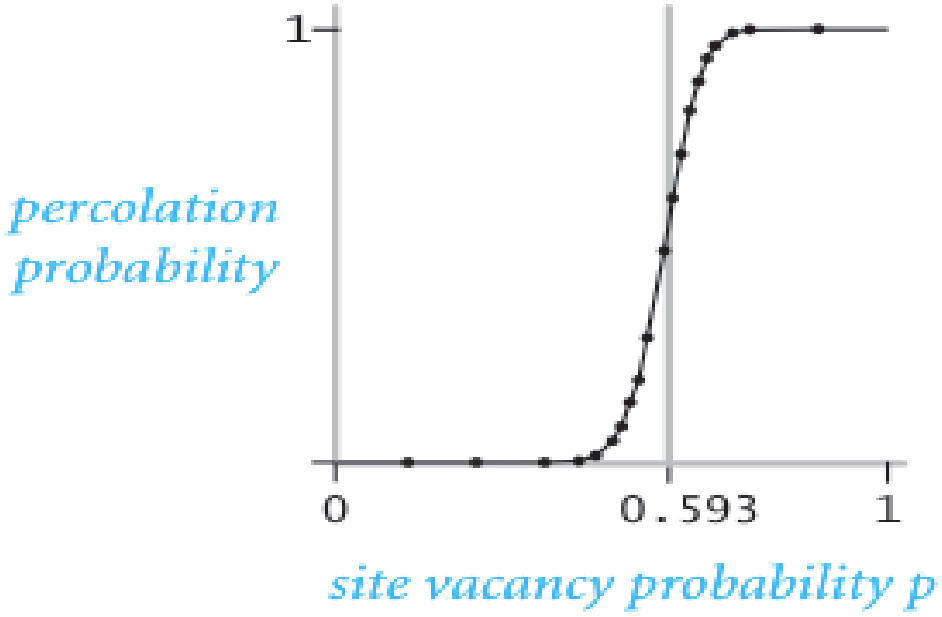

Fig. 5.11 – The Chances of Percolation in a Finite System as a Proxy for Permeability (Bob Sedgewick 2008)

In order to mimic the shale reservoir, we once again match on pore size distribution as well as porosity. We use the same Rayleigh distribution for pore size shown earlier in Figure 3.8 to determine individual pore sizes. Figure 5.12 below shows the pressure profile for one realization of the 50 sphere 10X10X10 case. The porosity of this system is 31.1% and hence does not reflect the known topology of the shale system.

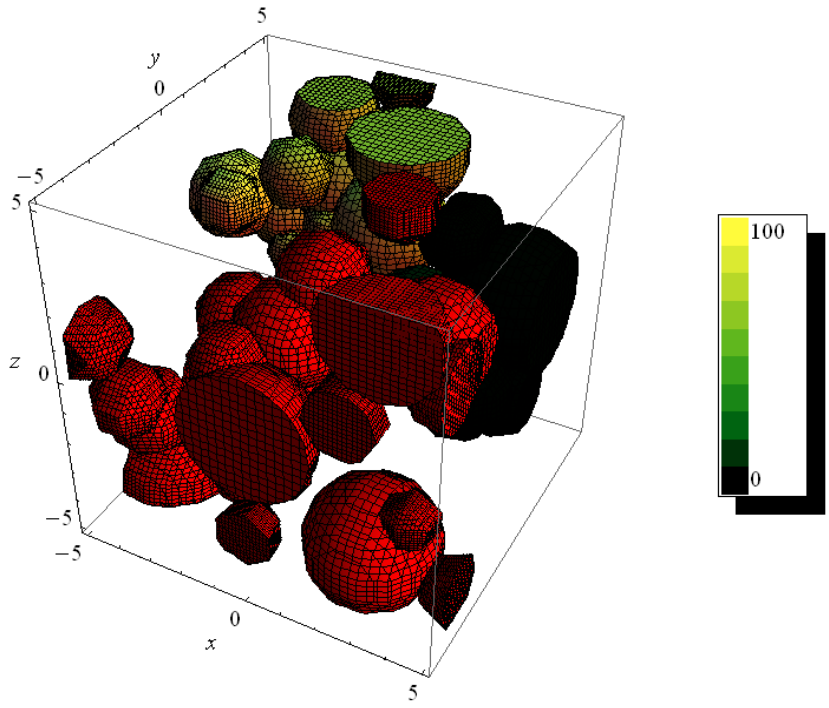

Fig. 5.12 – Rayleigh Distribution of Pore Radii at 31.1% Porosity. Demonstrates Large Scale Connectivity

Next, we must match on total system porosity between 4%-8%. We see in Figure 5.13 below that when matching on both pore size distribution and total system porosity we do not reach the percolation threshold.

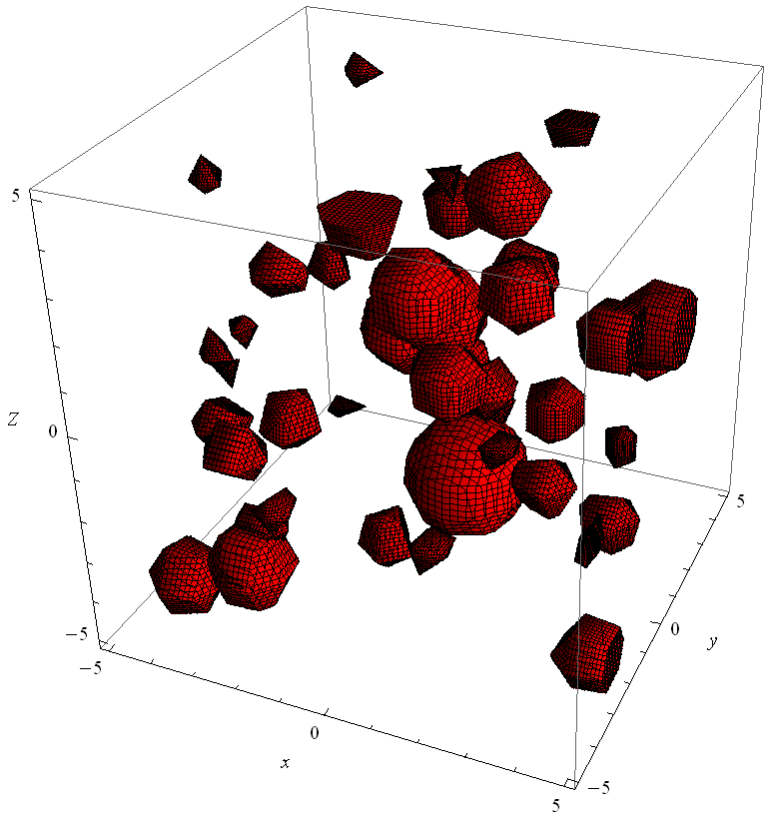

Fig. 5.13 – Rayleigh Distributed Pore Radii at 5.3% Porosity. Demonstrates a Lack of Large-Scale Connectivity

The result in Figure 5.13 above is consistent with our understanding of excluded volume discussed earlier. We recall that the ideas of excluded volume led us to conclude that percolation porosity of spheres is invariant under varying radial distributions. As a result, we would generally expect that systems below 29% porosity would not percolate, regardless of radial length distribution while those above 29% would percolate. This fact is anecdotally confirmed by simulation as shown in Figures 5.7 and 5.12 above.

CONCLUSIONS

The 3 dimensional continuum models demonstrate several key facts about the shale system. First, they allow us to confirm our finding with those from excluded volume. We saw that spherical systems do not percolate below 29% porosity as was shown by excluded volume and that the spherical system percolation porosity is invariant under any distribution in pore radius length.

Second, we see the effect percolation porosity has on total system permeability. In order for large scale connectivity to occur in the system, we saw that large pore shape anisotropy was a necessary condition. However, the increase in anisotropy caused a similar decrease in permeability. As the shale system is defined by extremely low permeability, the presence of large aspect ratio pore spaces would seem to explain the low permeability phenomenon.

Finally, we are able to make estimates concerning the amount of connected pore volume to the percolating cluster. We saw in Figure 5.1 that even above the percolation threshold at 32% porosity for the spherical system, roughly 1/3 of the total pore space was stranded (unable to communicate with the percolation cluster). In the case of higher aspect ratio shapes, which we determined were a necessary condition for percolation in a shale system, we see that this number gets even higher, leaving larger and larger percentages of pore space stranded.

In terms of shale reservoirs, this fact has a profound impact on the amount of accessible fluids. Even if porosity is high, it appears likely that this is not effective porosity. Despite reservoirs having a large amount of fluids in place, a large portion of those will likely not be accessible.

CHAPTER VI

TIME OF FLIGHT

MODEL THEORY

Time of flight (TOF) is a concept that describes the time it takes for an object or phenomena to move through a system. There are two types of TOF often utilized in the discussion of porous media. The first is convective TOF. This refers to the speed in length divided by time with which an individual particle moves in the system. The second, and the one we are generally concerned with when discussing reservoir characteristics, is diffusive TOF. This refers to the speed at which a pressure wave moves through a system or in our case, a shale reservoir. We apply both forms of TOF to the 3 dimensional continuum models constructed in the previous section.

In order to construct a TOF profile it is first necessary to build what is termed a cost function. The function delineates the time it takes either a fluid particle or pressure wave to move from point A to point B or in our simulations, from sphere A to sphere B. This cost function is determined for every connected sphere pairing in the simulation.

In order to determine arrival times for every sphere we employ Dijkstra's algorithm whether we are examining convective TOF or diffusive TOF systems (Dijkstra 1959). Dijkstra's algorithm is a shortest path algorithm that operates by constantly updating the arrival times of each node in the system. In our system, a node would be each sphere center. To begin, every node except the initial nodes is set to an arrival time of infinity while the initial nodes are set to arrival times of zero. The cost function then determines the arrival time to each node that is connected to the initial nodes. The node with the shortest arrival time is advanced to and each node's arrival time is then updated as the arrival time of the previous node plus the cost of moving from the previous node to the current one. The process is then repeated. Once a node is advanced to, it can never be revisited. Through this method, all connected nodes' arrival times are eventually calculated and a pressure wave arrival time profile can be determined. By employing Dijkstra's algorithm with the cost function for diffusive TOF we obviate the need for a pressure solve, allowing for very fast calculation of arrival times.

In addition to the arrival time we also aim to determine the volume encompassed by the pressure wave as it moves through the system. This displays invaded reservoir volume as a function of time by adding the incremental volume for each new sphere, minus any sphere overlap, for each step in Dijkstra's algorithm. As a result, we maintain a list of arrival time versus system volume that can later be examined.

The construction of the more conceptually familiar convective TOF cost function is straight forward. We recall that by determining the pressure profile of the system, we were also able to determine the flow profile (i.e. the volumetric flow rate and flow direction are known for every sphere). Because convective TOF is based simply on the speed the fluid moves in a media, constructing a fluid velocity profile only requires dividing the volumetric flow rate between adjoining spheres by the cross sectional area of their overlap (i.e. the area of the pipe normal to the flow direction connecting the two spheres). The example below (Fig. 6.1) is used to validate the TOF simulator and demonstrate important simulator properties. We have seen a similar construction in the development of the pressure solver for the continuum case in earlier sections. Once again, we use a horizontally aligned set of 10 percolating spheres in the usual 10X10X10 construction with sphere radii equal to 0.95.

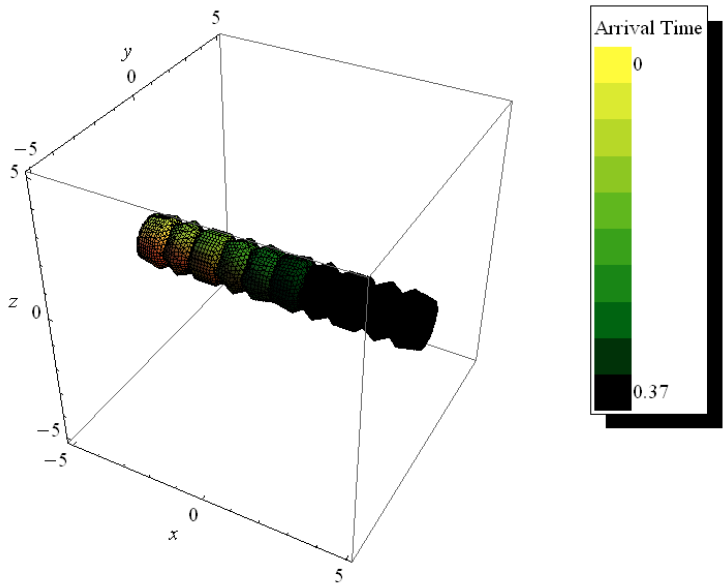

Fig. 6.1 – Validation of Convection TOF Model Using Horizontally Aligned Spheres

Figure 6.2 below shows volume growth in the system as a function of time. In other words, it displays the volume a fluid particle "sees" as it moves from the left to right outer boundaries of the system. We notice in this simplified example that volume growth is linear. This is expected because for each time step we are adding the volume of one more sphere. Additionally, all time steps are equal because the system is symmetric.

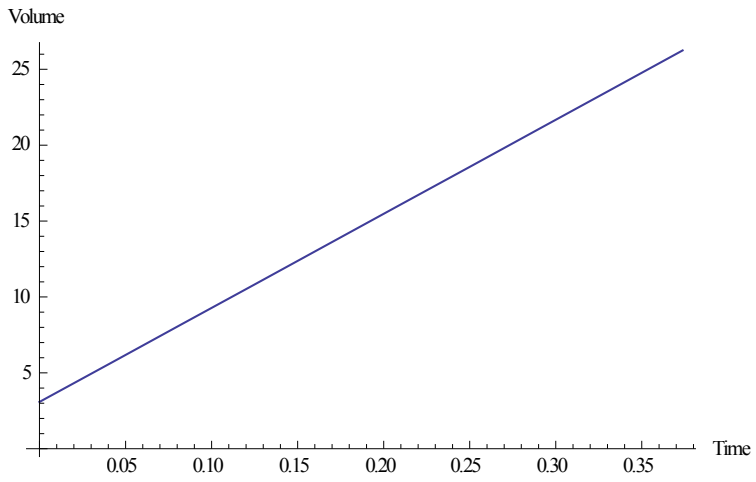

Fig. 6.2 – Volume Growth Versus Time in Convective TOF Validation Model

We can separately validate the volume results by calculating the volume of invaded pore space in the system. As done previously, we use Monte Carlo simulation to determine system porosity and percentage of invaded pore space. System porosity is 2.622% with 100% of pore space invaded. This yields a total invaded volume of $0.02622 * 1 * 10 * 10 * 10 = 26.22$. We compare this result to those shown graphically in Figure 6.2 where maximum volume occurs at approximately 26. They appear to be in good agreement.

Additionally, we note the added time necessary to compute convective TOF. As stated earlier, convective TOF requires a pressure solve in order to calculate flow rates. This process becomes prohibitively expensive in large systems. As we will see below, diffusive time of flight does not require a pressure solve, and hence is far more efficient at determining reservoir properties.

The derivation of the cost function for diffusive TOF is somewhat more involved. We derive our cost function from that of radius of investigation, where

$$t = \frac{* \mu * c_t}{6 * k} * r^2$$

t is time, μ is viscosity, c_t is total compressibility, k is permeability and r is the radius of investigation. In order to determine incremental distance, r, we take the square root of both sides which yields

$$\partial\sqrt{t} = \sqrt{\frac{* \mu * c_t}{6 * k}} * \partial r$$

We can then determine the incremental time it takes to move between any two pore spaces in our model. For instance, assuming $= \mu = c_t = 1$ leaves

$$\partial\sqrt{t} = \sqrt{\frac{1}{6 * k}} * \partial r$$

From here, k is determined as the transmissibility between any two spheres (as previously shown) and r the distance between sphere centers. We are then able to determine the time it takes a pressure wave to move the incremental distance r.

This time is calculated for every connected sphere pairing in the system in the development of the cost function. The cost in this case is the time it takes the pressure wave to move from one sphere to the next.

We note some general characteristics that result from this equation. The first is that any two non-intersecting spheres have transmissibility zero, which leads to a transit time of infinity as one would expect. Spheres that never intersect the percolating cluster have infinite arrival times. Additionally, the larger the permeability the faster the transit time will be. Hence, spheres along the main cluster will quickly lose pressure while those along the outer edges will take longer times to reach pseudo steady state. Efficacy of the diffusive TOF simulator is shown below (Fig. 6.3) as was with the convective case.

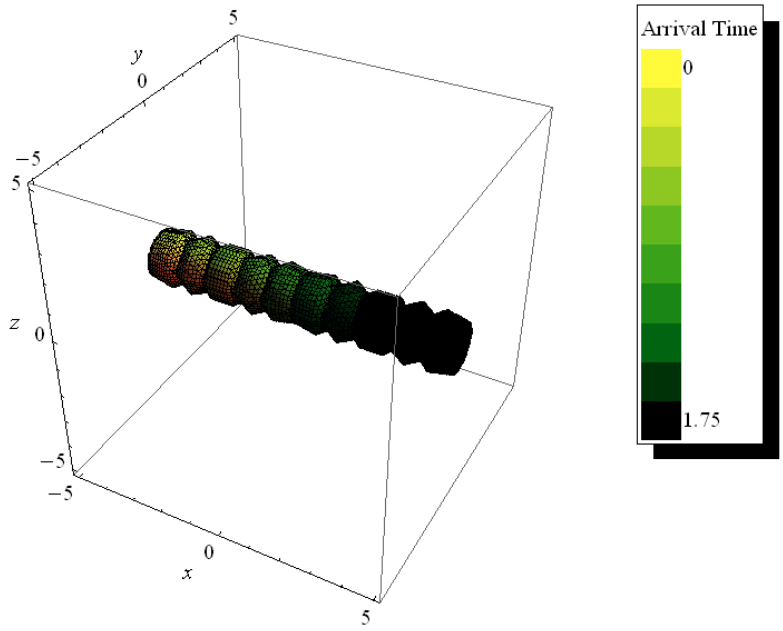

Fig. 6.3 – Validation of Diffusive TOF Model Using Horizontally Aligned Spheres

Additionally, we look at volume growth in this system as shown in Figure 6.4. As is expected, total volume exactly matches that for the convective TOF case. Arrival time for each volume level and maximum volume is the only difference between the convective and diffusive case.

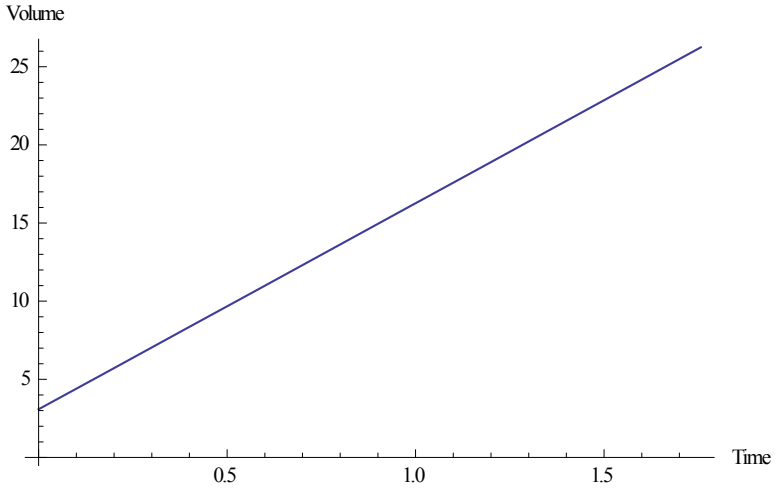

Fig. 6.4 – Volume Growth Versus Time in Diffusive TOF Validation Model

TOF SIMULATIONS

Convective

We begin with a small 50 sphere system in the usual 10X10X10 construction. The figure below (Fig. 6.5) shows the arrival time profile for the system. Because transmissibility between adjacent spheres is not held constant, we see the volume growth over time is also not constant as shown below in Figure 6.6. Instead, because of the limited size of the system, we see a stair step increase in volume as each sphere volume is added to the system. Once again we are moving left to right along the x-axis where $x = -5$ is the high pressure, left boundary and $x = 5$ is the low pressure, right boundary. Spheres not connected to the percolating cluster are left as red.

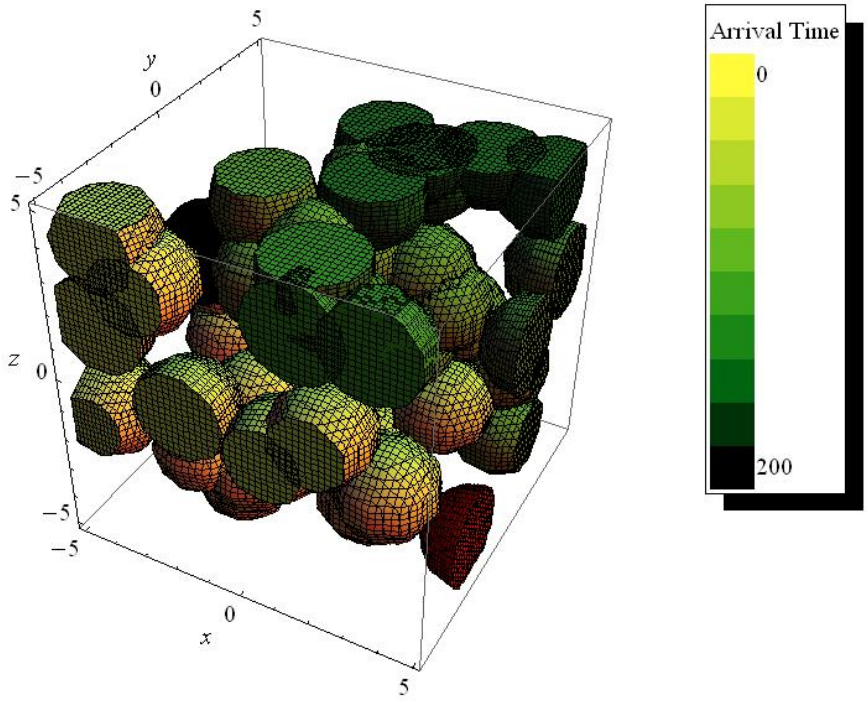

Fig. 6.5 – Arrival Time Profile for Convective TOF in a 50 Sphere Realization

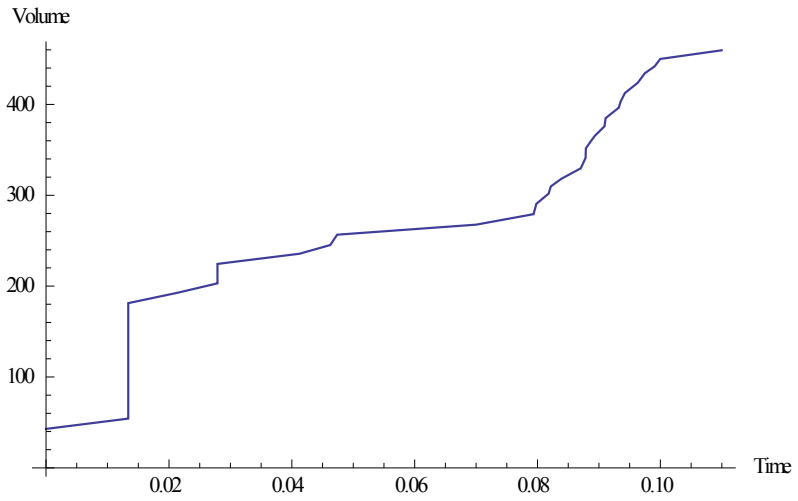

Fig. 6.6 – Volume Growth as a Function of Time Using 50 Spheres. Stair Step Volume Growth is the Result of Finite Size Steps.

Additionally, able to separately verify the total volume of the pore space invaded and compare it to the volume determined above. Using the same Monte Carlo methods given in the previous section we see approximate porosity is 23.23% with 89.5% of the pore space invaded. This results in an invaded volume of approximately 437.7. When comparing this to the maximum volume value shown in the graph above as approximately 450, we see that they in good agreement.

Due to the pressure solve requirement for convective TOF, determination of a TOF profile is computationally infeasible to examine extremely large systems. However, the volume growth profile shown below (Fig. 6.7) shows a 500 sphere realization with radius 0.8 in the usual 10X10X10 construction.

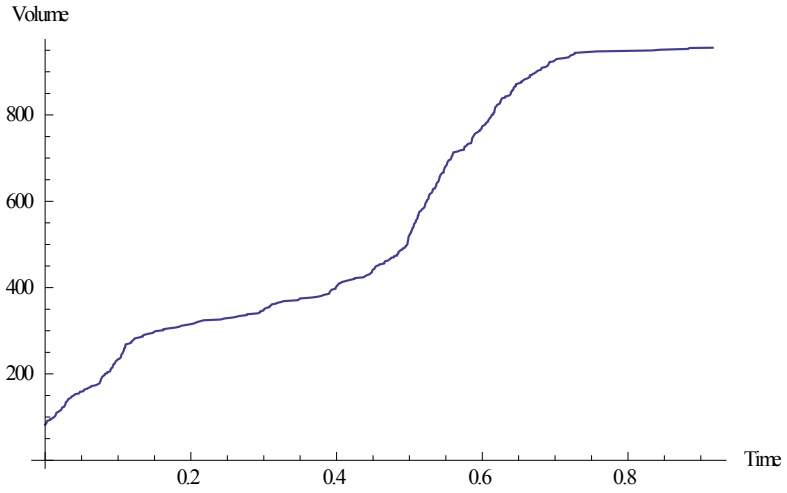

Fig. 6.7 – Volume Growth as a Function of Time Using 500 Spheres. Smoothing out of the Stair Step Occurs as the Number of Spheres Increases.

Once again, we compare total volume in the chart with Monte Carlo solutions. This system is approximately 33% porous with 93% of the pore space invaded. As a result, the total volume is approximately 920 with Monte Carlo methods which is in good agreement with the graph above.

Diffusive

We begin in the same manner as we did for convective TOF models by showing a 50 sphere realization. The figures below show the TOF profile as well as the volume growth profile. Once again we see the characteristic stair step pattern due to finite size effects.

Next, we look at a larger scale, single porosity model. By single porosity we are referring the fact that there is only one pore (sphere) size. The graph below (Fig. 6.8) shows the characteristic volume growth in a single porosity (conventional reservoir system) during the transient phase.

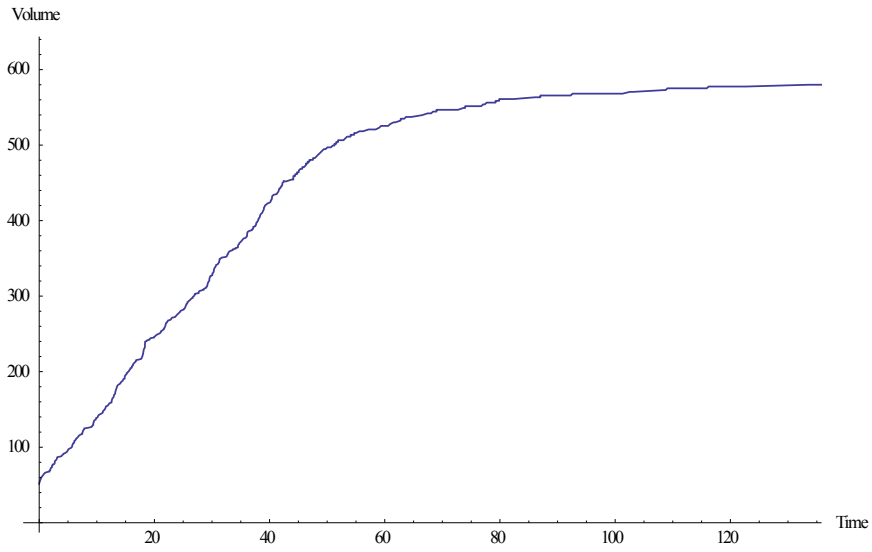

Fig. 6.8 -750 Spheres of Equal Size, 46.34% Porous

We then move to two dual porosity models to examine the volume growth profile. Two different types of dual porosity systems are examined. The first, as displayed below (Fig. 6.9), shows large spheres as well as small spheres of 1/512 the volume randomly placed throughout the system.

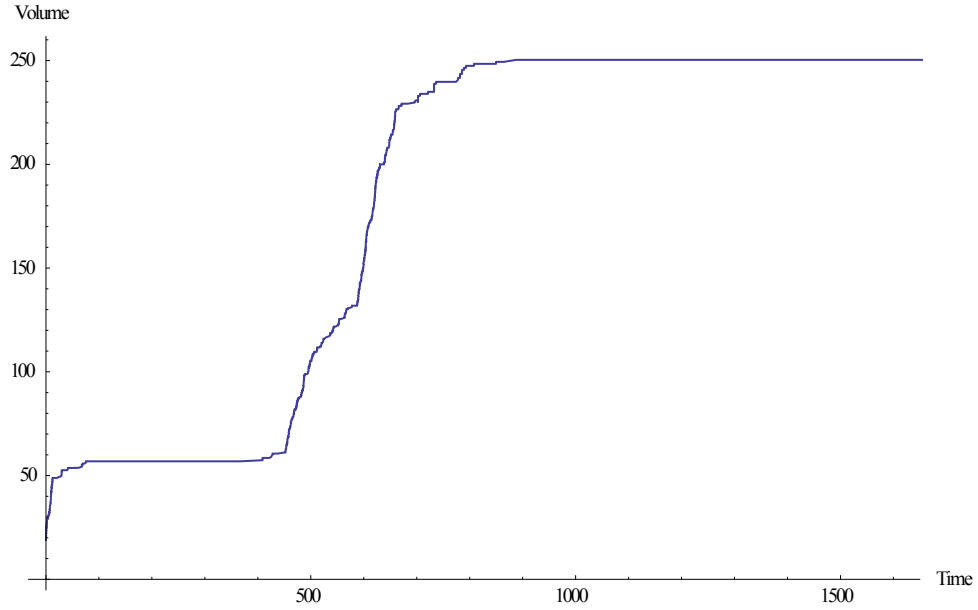

Fig. 6.9 - 750 Large Sphere, 3750 Small at 1/8 Radius, 47.1% Porous

Because of low transmissibility in the large-small sphere interaction and the small-small sphere interaction, we see a large amount of volume growth in late time. This is characteristic of a dual porosity system and expected as it is difficult for the pressure wave to move further into low permeability zones.

The second dual porosity model has a fixed geometry as shown below (Fig. 6.10). This model shows a similar volume growth profile but has more defined periods of growth as shown in Figure 6.11 below.

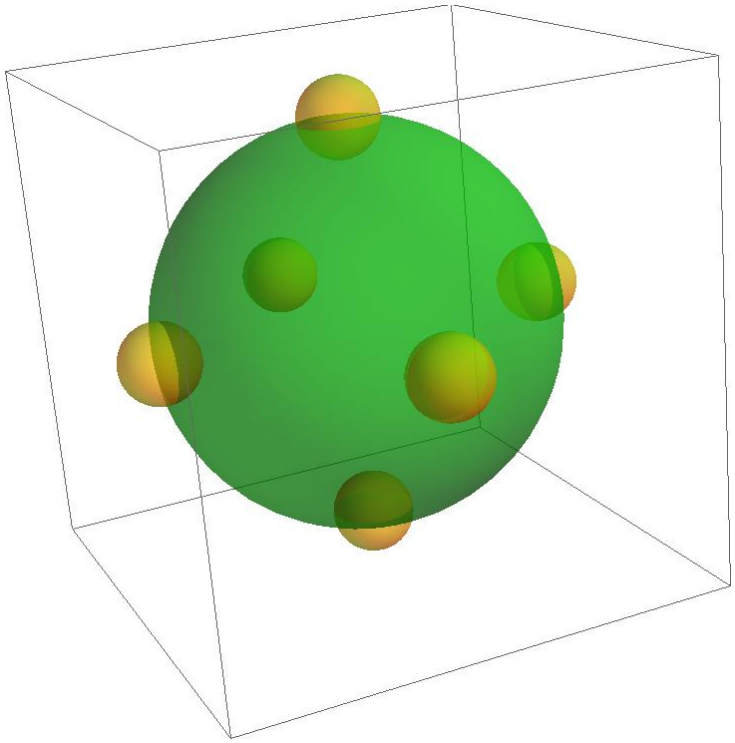

Fig. 6.10 – Geometry of the Dual-Porosity System. Smaller Spheres of 1/8 Radius

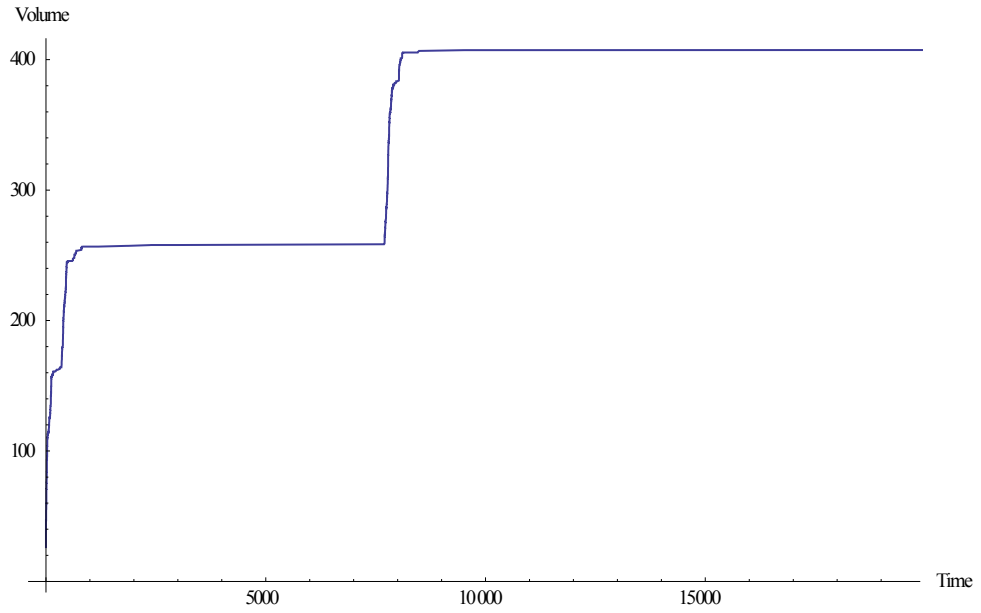

Fig. 6.11 - 750 Spheres, 4500 Small Attached Spheres. 33.93% Porous

Once again this shape is characteristic of a dual porosity system. The pressure wave quickly moves through the relatively high permeability zones of the large, well connected spheres and takes much longer to move into the low transmissibility small spheres.

CONCLUSIONS

We begin by making several qualitative assessments of volume growth and its relation to pressure decline within the unconventional system and finish with suggestions for future work to better understand the nature of volume growth as it relates to rate decline in unconventional systems.

First, we see that volume growth is dominated by transmissibility. Hence, the larger the transmissibility the faster a pressure wave is able to move through the system. In a system right at the percolation threshold, the vast majority of connected pore space exists as the “backbone” of the percolating cluster. This “backbone” pore space is very well connected and generally allows for rapid pressure depletion. As the system moves away from the percolation threshold, more pore space is connected to the “backbone” through increasingly tortuous paths. The addition of these long path, long times of flight in high tortuosity clusters causes slower pressure depletion and as a result, slower rate depletion.

We see that large volume growth at late time is characteristic for the large scale, dual porosity simulations shown above. This late time volume addition is the result of tortuous paths having been taken in order to access additional pore space. This is likely the mechanism by which large volumes of relatively low, but stable rate gas come from unconventional resources in late time (Bowker 2007).

A full comparison of the percolation model with empirical rate decline in unconventional reservoirs is left for later study; however, understanding the cluster characteristics of volume growth within a percolating or non-percolating system can shed light on the nature of rate decline. The following chapter examines the characteristic time for individual clusters to reach pseudo-steady state and that time's relation to the stretched exponential function.

CHAPTER VII

CONCLUSIONS

RELATIONSHIP TO THE STRETCHED EXPONENTIAL

The case was made earlier that the shale gas system is likely below the percolation threshold. As a result, there exists a distribution of finite cluster sizes that make up the connected space of the system. Within this distribution of clusters, a certain percentage will be connected to the reservoir's induced fracture network and a certain percentage will be stranded. As the pressure wave moves down the fracture network or "backbone" of the percolation cluster it will encounter these clusters at varying times. Once a cluster has been reached by the pressure wave, exponential pressure depletion in that cluster will begin. Because the size and topology of each cluster will vary according to the connectivity of the reservoir in question, the time it takes the pressure wave to reach the boundary of each cluster will also vary. Assuming an average cluster size can be defined according to a certain distribution of cluster sizes within the system, then an average exponential time decay time can also be defined. Because of the varying arrival times of the pressure wave at each cluster and our ability to define an average decay time for each cluster, we see that the reservoir a system of exponential declines in pressure which are overlapping through time. This could be the basis for the stretched exponential decline curve as observed by Valko and Lee (2010), where the τ and η constants are a function of the average cluster size. Namely, it is possible that τ is the characteristic time for the average cluster size to move to pseudo steady state.

CONCLUSIONS

We saw that while the initial on-lattice models were accurate in measuring the characteristic exponent of several systems, it was difficult to properly simulate the shale geology. As a result the 3D continuum model was developed that could accurately mimic a shale system. The 3D continuum model allowed us to validate our findings from excluded volume concerning the percolation porosity of a system as well as the fundamental effect of shale pore shape anisotropy of percolation porosity. While we did not develop a continuum model that exactly matched those qualitatively seen in the shale SEM images, we were able to provide several possible solutions to how shale systems develop permeability.

Most striking in our exploration of excluded volume was the role pore shape anisotropy plays in percolation porosity. High aspect ratio pores determine connectivity and hence permeability in shale systems. One result of this is the likely fact that in-situ, pre-stimulation shale is below the percolation threshold. It is only by introducing high aspect ratio pores (fractures) to the system that large scale connectivity is obtained.

Additionally, we saw that the dual or multiple porosity system is a likely candidate to describe the shale pore network. The volume growth profile of the dual pore system provides a possible mechanism by which shale gas wells have dramatic rate decline in the first few years, but still allow for large volume of relatively low rate gas for extended periods of time. In addition to the dual porosity systems that were examined in this paper, it is likely that multiple porosity or fractal models provide a more accurate glimpse into the true volume growth within a shale reservoir. These questions however are left for later work.

Additionally, we examine the likely cases that a shale system is just below or just above the percolation threshold. We want to know whether specific shale's location just above or just below the percolation threshold has a profound effect on the deliverability of hydrocarbons from that formation. First, we examine the case where we are just below the percolation threshold. In this case, the average cluster size in the system in just below infinity. Even though we do not have large scale connectivity in the system, we will still encounter large cluster during the drilling and stimulation processes. This means that the well encounters near infinite clusters that will allow for pressure depletion and flow. As a result the system can be below the percolation threshold and hence have no permeability on a large scale, but still have access to large quantities of hydrocarbon. Second, the system slightly above the percolation threshold yields a similar result. In this case, the cluster that drilling and stimulation encounter is likely to be of infinite number of pores and hence, have large amounts of accessible hydrocarbon.

Even if we know where a certain shale reservoir exists in relation to the percolation threshold, can we predict how well that system will then produce? It seems likely that there are 3 classifications of quality that the shale reservoirs can be lumped into in regards to their levels of connectivity. The first and best class would be those systems that are well above the percolation threshold. Generally, they would be characterized by high TOC and brittle shale that allows for large, high aspect ratio fractures. This group would nearly always be economically exploitable. The second group would be those shale systems right at the percolation threshold. These systems

would likely be characterized by more elastic shale that did not produce as high of levels of connectivity. These systems may or may not be economically exploitable because of exactly how the fracture network is induced in the shale. Finally, a third group of shale well below the percolation threshold would be characterized by low TOC and elastic shale. Elastic shale does not allow for high enough aspect ratio pores to be generated as the fracture likely builds too much length in the direction normal to fracture propagation. As a result, these plays will likely never be economically exploitable. In summary, not all shale is created equal and several factors including TOC and more importantly fracture shape anisotropy play a large role in their economic viability.

REFERENCES

Balberg, I. 1986. Excluded-Volume Explanation of Archie Law. *Physical Review B* **33** (5): 3618-3620.

Balberg, I., Anderson, C.H., Alexander, S. et al. 1984. Excluded Volume and Its Relation to the Onset of Percolation. *Physical Review B* **30** (7): 3933-3943.

Berkowitz, B. and Balberg, I. 1992. Percolation Approach to the Problem of Hydraulic Conductivity in Porous-Media. *Transport in Porous Media* **9** (3): 275-286.

Berkowitz, B. and Balberg, I. 1993. Percolation Theory and Its Application to Groundwater Hydrology. *Water Resources Research* **29** (4): 775-794.

Bob Sedgewick, K.W. Percolation. http://www.cs.princeton.edu/courses/archive/spr11/cos226/assignments/percolation.html . Accessed June 14, 2012.

Bowker, K.A. 2007. Barnett Shale Gas Production, Fort Worth Basin: Issues and Discussion. *The American Association of Petroleum Geologists* **91** (4): 523-533. DOI: 10.1306/06190606018

Curtis, M.E., Ambrose, R.J., Sondergeld, C.H. et al. 2011. Transmission and Scanning Electron Microscopy Investigation of Pore Connectivity of Gas Shales on the Nanoscale. Paper presented at the North American Unconventional Gas Conference and Exhibition, The Woodlands, Texas, USA. Society of Petroleum Engineers SPE-144391-MS. DOI: 10.2118/144391-ms.

Curtis, M.E., Sondergeld, C.H., Ambrose, R.J. et al. 2012. Microstructural Investigation of Gas Shales in Two and Three Dimensions Using Nanometer-Scale Resolution Imaging. *Aapg Bulletin* **96** (4): 665-677. DOI: Doi 10.1306/08151110188

Darcy's Law and Applications. Scribd. http://www.scribd.com/doc/44698468/Darcy-s-law. Accessed June 4, 2012.

Dijkstra, E.W. 1959. A Note on Two Problems in Connexion with Graphs. *Numerische Mathematik* **1**: 269-271. DOI: 10.1007/BF01386390

Elgmati, M.M., Zhang, H., Bai, B. et al. 2011. Submicron-Pore Characterization of Shale Gas Plays. Paper presented at the North American Unconventional Gas Conference and Exhibition, The Woodlands, Texas, USA. Society of Petroleum Engineers SPE-144050-MS. DOI: 10.2118/144050-ms.

Ewing, R.P. and Horton, R. 2007. Thermal Conductivity of a Cubic Lattice of Spheres with Capillary Bridges. *Journal of Physics D-Applied Physics* **40** (16): 4959-4965. DOI: Doi 10.1088/0022-3727/40/16/031

Loucks, R.G. 2012. Spectrum of Pore Types and Networks in Mudrocks and a Descriptive Classification for Matrix-Related Mudrock Pore. *The American Association of Petroleum Geologists* **96** (6): 1071-1098. DOI: 10.1306/08171111061

Loucks, R.G., Reed, R.M., Ruppel, S.C. et al. 2009. Morphology, Genesis, and Distribution of Nanometer-Scale Pores in Siliceous Mudstones of the Mississippian Barnett Shale. *Journal of Sedimentary Research* **79** (11-12): 848-861. DOI: Doi 10.2110/Jsr.2009.092

Passey, Q.R., Bohacs, K., Esch, W.L. et al. 2010. From Oil-Prone Source Rock to Gas-Producing Shale Reservoir Â€ " Geologic and Petrophysical Characterization of Unconventional Shale-Gas Reservoirs. Paper presented at the International Oil and Gas Conference and Exhibition in China, Beijing, China. Society of Petroleum Engineers SPE-131350-MS. DOI: 10.2118/131350-ms.

Saar, M.O. and Manga, M. 2002. Continuum Percolation for Randomly Oriented Soft-Core Prisms. *Physical Review E* **65** (5). DOI: Artn 056131.Doi 10.1103/Physreve.65.056131

Stauffer, D. and Aharony, A. 1994. *Introduction to Percolation Theory*. London ; Bristol, PA: Taylor & Francis. Original edition. ISBN 0748400273.

Wang, F.P. and Reed, R.M. 2009. Pore Networks and Fluid Flow in Gas Shales. Paper presented at the SPE Annual Technical Conference and Exhibition, New Orleans, Louisiana. Society of Petroleum Engineers SPE-124253-MS. DOI: 10.2118/124253-ms.

Wesstein, E. Taylor Series. Wolfram. http://mathworld.wolfram.com/TaylorSeries.html. Accessed June 3, 2012.

Wesstein, E. Rayleigh Distribution. MathWorld - A Wolfram Web Resource. http://mathworld.wolfram.com/RayleighDistribution.html. Accessed June 2, 2012.

APPENDIX A

Description of Flow Simulator

The flow simulator determines pressure drop based on the transmissibility weighted average of pressures from surrounding cells in the steady state condition.

We begin with by stating the sum of the fluxes for each sphere is equal to zero (Flow in = Flow out),

$$Tl * (P1 - Pl) + Tb * (P1 - Pb) + Tr * (P1 - Pr) * \mathrm{Tt} * (\mathrm{P1} - \mathrm{Pt}) = 0$$

where T is the transmissibility at each face. T as derived from Poiseuille flow is given below:

$$T = \frac{\pi * r^4}{8 * \mu * D}$$

By prescribing a pressure at the left and right system boundaries as well as an initial pressure for each cell we can build a linear system, solving for the pressure at each cell.

Solving the above zero flux equation for P1 yields:

$$(Tt + Tb + Tl + Tr) * P1 - Pb * Tb - Pl * Tl - Pr * Tr = 0$$

Converting to matrix form for all cells we obtain:

$$TP = 0$$

$$T = \begin{bmatrix} \sum T & -Tr & 0 & \cdots \\ -Tl & \sum_{\cdots} T & -Tr & \cdots \end{bmatrix}$$

$$P = \begin{bmatrix} P1 \\ P2 \\ P3 \\ \cdots \end{bmatrix}$$

Finally, we employ the Gauss-Siedel iterative scheme until pressure convergence occurs.

Flow rates are then solved for via Poiseuille flow where a pressure gradient and transmissibility are known for each cell.

$$\Delta P = \frac{8 * \mu * D * Q}{\pi * r^4}$$

$$\Delta P * T = Q$$

We are looking at aggregate flow across the right face of the system and hence sum the flow across the entire right hand boundary.

VITA

Name: Ian Bernard Chapman

Address: Harold Vance Department of Petroleum Engineering
Texas A&M University
3116 TAMU – 407 Richardson Building
College Station, TX 77843-3116

Email Address: IBC8E@virginia.edu

Education: B.S. Physics and Mathematics, University of Virginia, Charlottesville, VA, USA, 2008
M.S. Petroleum Engineering, Texas A&M University, College Station, TX, USA, 2012